



Monograph

Modeling Curves Subject to a Bending Energy

C.A. Miermans
2015

Monograph
Modeling Curves Subject to a Bending Energy
version 2

Author:
Karsten Miermans
Supervisors:
Cornelis Storm
Remy Kusters

Compiled During:
22 December 2014—9 February 2015

Foreword

This written work is a monograph of the first five weeks of my graduate work (10 November–10 December 2014) at the group “Theory of Polymers and Soft Matter” at the department of Applied Physics, Eindhoven University of Technology. This graduate work is titled “On the Morphology of Dendritic Spines” as a part of my master’s degree in Applied Physics.

The first five weeks of my graduate work I worked on the bending of curves (using a Fourier representation). I have collected most of the work through my *laboratory journals*, which are quite extensive notes on my day-to-day progress.

I would like to take this opportunity to thank Remy and Kees, who have both been a great source of inspiration during this project. I feel that their enthusiasm and expertise have been indispensable for me. I am looking forward to the road ahead, and our cooperation in the future. Moreover, I would like to express my deep gratitude to my family and my beloved girlfriend. I do not—and cannot—express my love to you often enough.

Contents

1	Introduction	3
1.1	Research Questions	3
1.2	Boundary Conditions and Constraints	4
2	Theory	5
2.1	Curvature Energy as a <i>Landau Theory</i>	5
2.2	Series Solutions to an Energy Functional	6
2.3	The Tangent Vector	7
2.3.1	Enforcing Normalization onto $T(s)$	7
2.4	Expansions of Bending Beams	9
2.5	Implementation of Boundary Conditions and Constraints	10
2.6	Energy of Fourier Expansion	11
3	Results	12
3.1	Shapes	12
3.2	Quantitative Analysis of Shape Morphology	15
3.2.1	Energy Landscape of Shape Growth	15
3.2.2	The Power Spectral Density—Which Length-Scales Matter?	17
3.2.3	Shape Height, Head and Neck Width	19
3.2.4	Shape Volume	20
3.3	Dynamics of Shape Growth	21
3.3.1	Dynamics Due to a Potential Landscape	22
3.3.2	Dynamics Due to a Potential Landscape, Including a Growth Term	23
3.3.3	Dynamics Due to a Potential Landscape, Including a Growth Term and a Growth Inhibition Term	24
3.4	Validity of Results	26
3.4.1	Stability	26
3.4.2	Convergence	29
3.4.3	Comparison with Finite Difference Method	30
4	Conclusion and Outlook	32
4.1	Summary of Findings	32
4.2	Outlook	33
A	Minimization Algorithm	36
B	Plateau Regime in Energy Spectrum	39

Chapter 1

Introduction

The order of the monograph is as follows: I will first lay out some preliminary considerations with regards to the system that we are examining. Then, we will discuss some of the general aspects of the theory (series solutions, Fourier-series). After that, for the most important part: the results. In the Results chapter, we will also discuss the stability, convergence and validity of the method. Finally, a summary of the work and how this relates to possible future work is presented in the chapter “Conclusion and Outlook”.

Why are we *überhaupt* discussing curves that resist bending? For one thing, it is because many well known biological systems in Nature have this property. The ‘systems’ we are referring to here are very slender—and as such, can be modeled as curves. Examples of slender objects are: DNA, microtubuli, ...¹. But, more important for us (than the *direct* biological relevance) is to model structures called *spines*. These spines are membranes that are present in the brain, and are the central object of investigation in my graduate work. Although spines are *two-dimensional* structures (as opposed to curves, which are one-dimensional), this work serves as a way for us to test the Fourier method that we will developing. This testing, in turn, is done because the modeling of two-dimensional structures is far more difficult. In summary: We hope to develop a method-based on a Fourier series approximation—that we can also use for modelling membranes.

1.1 Research Questions

In chapter 2 we will discuss some of the theoretical aspects of this work. But before we delve into those details... Why are we actually discussing it at all? More to the point: What are we hoping to achieve in this work? To this end, we have formulated several research questions we are hoping to answer:

- What types of shapes are associated with curves that minimize their bending energy? Will there be formation of a head and neck? Will the shape be self-crossing?
- If we allow a shape to grow or shrink freely, how will it evolve? Will there be only one possible evolution, or a bifurcation of shapes? Will there be a critical arc-length that has to be overcome for the shape to grow spontaneously?
- How can we model exocytic processes?² What is their importance with respect to shape stability?

¹According to Wikipedia, DNA is about 85 times longer than it is wide, and microtubuli can be up to 1000 times longer than they are wide.

²For a beautiful overview with many illustrations of biological processes, take a look at Phillips et al. [18]. In particular, vesicle fusion is illustrated on page 459.

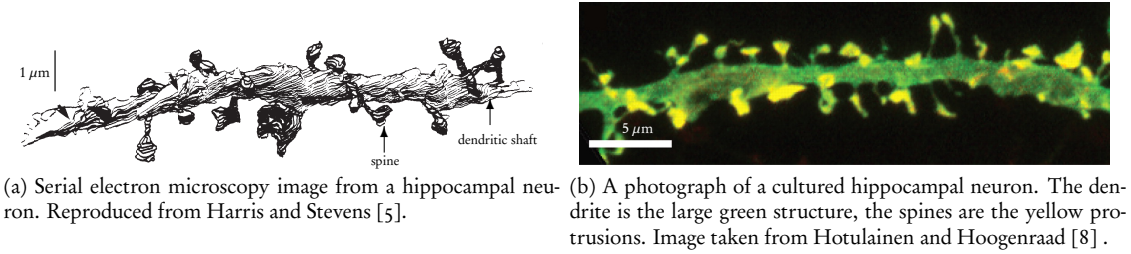


Figure 1.1: Images of hippocampal neurons as published in 1989 (left) and 2010 (right).

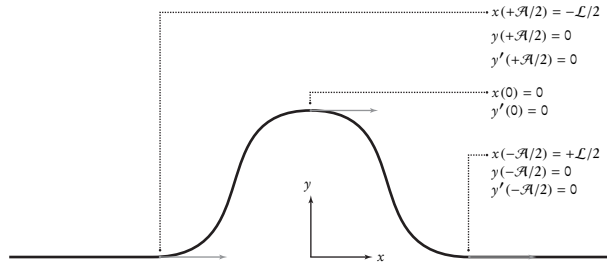


Figure 1.2: Schematic of the geometry involved, along with the boundary conditions.

1.2 Boundary Conditions and Constraints

We will investigate the problem of curves that resist bending using a Fourier expansion given in equations (2.2), (2.3). In order to minimize the energy functional we also require boundary conditions. The boundary conditions we will use are inspired by the geometry of spines that lives on a dendrite. The dendrite is namely a relatively macroscopic structure that enforces the spine structure to be an out-of-plane deformation. This is quite clear from a fluorescent image of a dendrite, shown in figure 1.1b. Also, some beautiful serial electron microscopy images have been produced by Harris and Stevens [5] as early as 1989, one of which has been reproduced in figure 1.1a. This image also shows that the spines can be approximated by out-of-plane deformation with respect to the dendritic shaft.

Inspired by these observations from biology, we devised boundary conditions that have been displayed in figure 1.2. The boundary conditions are thus:

$$x(0) = 0, \quad (1.1)$$

$$x(\pm A/2) = \pm L/2, \quad (1.2)$$

$$y(\pm A/2) = 0, \quad (1.3)$$

$$y'(\pm A/2) = 0, \quad (1.4)$$

$$y'(0) = 0. \quad (1.5)$$

The fact that the tangent vector is normalized makes $x'(s)$ and $y'(s)$ connected through $x'(s)^2 + y'(s)^2 = 1$. Enforcing this last statement is not trivial. Remember that we represented $x(s), y(s)$ both as Fourier series of order n , so there have to be $2n$ equations solved. We will discuss this matter in detail in section 2.3.1.

Chapter 2

Theory

2.1 Curvature Energy as a *Landau Theory*

We will consistently describe the amount of ‘bending’, which is an informal statement, by the rate of change of the tangent vector. The tangent vector will be written $\mathbf{T}(s)$, where s is the arc-length across the curve—the ‘bending’ can then be written $d\mathbf{T}/ds$.

Now that we have found a way to classify systems based on the amount of ‘bending’, a natural question is to ask:

“Can we devise a formula that tells us how much *energy* is associated with a certain value of $d\mathbf{T}/ds$? ”.

Well, let’s try and *guess* such a formula. Suppose we first propose that the energy \mathcal{E} associated with some amount of ‘bending’ can be described by the following formula:

$$\mathcal{E} \stackrel{?}{=} K \int ds \left(\frac{d\mathbf{T}}{ds} \right),$$

where K is a constant. We can easily dispute this functional. For if we rotate the framework we are working with π radians, then $d\mathbf{T}/ds$ (and hence, \mathcal{E}) flips in sign—so this formula is in contradiction with rotational invariance of free space, one of the most deeply held beliefs in physics.

Another guess might be

$$\mathcal{E} \stackrel{?}{=} K \int ds \left(\frac{d\mathbf{T}}{ds} \right)^2,$$

where K is again a constant. This formula doesn’t suffer from the problem stated above. In fact, if we write $K = 2K_b$ this functional has a name: the *Canham-Helfrich functional*, and was already described in 1973 by Helfrich [7]. The constant K_b is, then, called the *bending rigidity*. As can be seen from the formula, K_b has dimensions of energy \times length. Loosely speaking, for a ‘high’ value of K_b (all other things being equal), only ‘large’ length-scales will be present in a system.¹ From this perspective, we might regard K_b as a measure for the *typical length-scale* of a system that is subject to a bending energy. The other way round, we might also say that K_b sets the *energy scale* for particular length-scales. These two views are, of course, entirely equivalent. The bending rigidity K_b of microtubuli is in the order of $\ell_p k_B T$, where ℓ_p is the *persistence length* in the order of millimeters [3; 22; 11; 16; 1], and that of DNA is

¹I should stress that I’m speaking of the *typical length-scale*, not the typical deformation size, which is an entirely different quantity. In fact, a ‘high’ value for K_b will only allow ‘small’ deformations.

in the order of nanometers [4]. We therefore expect that the bends in these curves are also in the order of millimeters for microtubuli, and in the order of nanometers for DNA.

Expressing the energy in terms of the function (dT/ds) is essentially a second-order *Landau theory* in the ‘order parameter’ (dT/ds) . Landau originally developed the theory to model the phase transition from gases to liquids [12], but the basic idea can be applied to the energy functional of any system. Henceforth we will take this expression for the energy to be exact, and investigate which functions $\mathbf{T}(s)$ minimize the bending energy. Let’s conclude, then, with our *definition* of the energy that we will be discussing:

$$\mathcal{E} = 2K_b \int_{\mathcal{M}} ds \left(\frac{dT}{ds} \right)^2 \quad (2.1)$$

2.2 Series Solutions to an Energy Functional

Suppose we have an energy functional

$$\mathcal{E}[\mathbf{T}(s)] \equiv \int_{\mathcal{M}} ds \left(\frac{dT}{ds} \right)^2,$$

where $T(s) \equiv dr/ds$ is the tangent vector to the curve and ds is the differential arc-length. Here we ignored the uninteresting factor $2K_b$, since for now our energy functional only has the one term anyway. The integration domain $\mathcal{M} = [-\mathcal{A}/2, +\mathcal{A}/2]$ is the part of the beam that we are investigating. Now, suppose we expand the coordinate vector $r(\tilde{s})$ (where $\tilde{s} \equiv s/\mathcal{A}$ is the reduced arc-length) using a series solution:

$$\begin{aligned} r(\tilde{s}) &\equiv \{x(\tilde{s}), y(\tilde{s})\}, \\ x(\tilde{s}) &\equiv \sum_k \alpha_k \phi_k(\tilde{s}), \\ y(\tilde{s}) &\equiv \sum_k \beta_k \phi_k(\tilde{s}), \end{aligned}$$

where the α_k, β_k are coefficients and the $\phi_k(\tilde{s})$ are basis functions, $\tilde{s} \equiv s/\mathcal{A}$ is the reduced arc-length. The reduced arc-length is a number $0 \leq \tilde{s} \leq 1$. We will be using real-valued coefficients and basis functions. The attentive reader might notice that we are using the same basis functions $\phi_k(\tilde{s})$ for both the x - and y -coordinates. The reason for this apparent restriction is that the energy functional that we are trying to minimize doesn’t discriminate between the x - and y -direction. One says that this particular energy functional is *rotation invariant*. Loosely stated, this is the observation that a membrane doesn’t care whether you have it point upside or downside.

There is a plethora of expansion schemes “out there”. To name just a few: Fourier series, Legendre polynomials, Hermite polynomials, Bessel functions, ... [20]. Polynomial expansions are not suitable for us, however, for the following reason: Any of the terms $\sim \tilde{s}^k$ in the expansion has second derivative $k(k-1)\tilde{s}^{k-2}$. And since $\tilde{s} \leq 1$, this will in general be a very small number. Hence, the coefficients will not necessarily converge, since only the *product* of coefficient and basis function has to converge.² In fact, experiments using a polynomial basis show that the coefficients will *diverge*. Hence, the interpretation of the coefficients is a mathematical procedure with little resemblance to the physics involved.

²Strictly speaking, this need not even be the case—and it might well be that one requires *all* of the terms in an expansion are required. We will not consider this complication.



Figure 2.1: A cartoon that illustrates the concept of stretch and contraction of an elastic band with marks on it. The number of marks on the elastic band is an invariant (five, in this case).

One expansion that is directly related to the physics involved is the *Fourier series*.³ A Fourier series probes the system of interest at specific *length-scales*. The basis functions in a Fourier series are written $\phi_k = \Omega_k e^{iks}$, where the wavenumber k is an inverse length-scale. These length-scales are intrinsically related to the boundary conditions. We will see that the possible modes will be related to the total arc-length of the curve, similar to stationary vibrations on a string. Furthermore, the Fourier series does not suffer from the problem of convergence stated in the previous paragraph. The energy of one such Fourier mode $\sim e^{iks}$ is namely $\sim k^4 |e^{iks}|^2$, and since k is not always a small number, this energy can be quite large. Hence, if we think about the system as one that minimizes its bending energy, we expect the coefficients to the higher-order modes to converge to zero.⁴

2.3 The Tangent Vector

The tangent vector $\mathbf{T}(s)$ is defined as follows: $\mathbf{T}(s) \equiv d\mathbf{r}(s)/ds$, where $d\mathbf{r}$ is the differential displacement vector and ds is the differential displacement. From the terminology of these quantities it is already clear that they are probably related. Well, the differential displacement is defined as $ds \equiv |\mathbf{r}(s+ds) - \mathbf{r}(s)| = |\mathbf{dr}(s)|$. Hence, we find that $|\mathbf{T}(s)| = |\mathbf{dr}|/ds = 1$. We summarize this in the statement:

The tangent vector is *normalized*.

Some authors use a different definition for the (differential) displacement, in particular in conjunction with curves that can be *stretched* or *contracted* (such as elastic bands). This different definition rests on the following idea: Suppose we mark the elastic band with N equidistant marks at distances Δ , and stretch, contract, and deform it in all sort of ways—the number of marks will remain N . We can define the total arc-length of the elastic band as $\Delta \cdot N$, which is an invariant for the elastic band. What this definition actually measures is the *rest arc-length* of the elastic band, or the arc-length of the elastic band in its *relaxed state*. We might define the tangent vector such that $|\mathbf{T}_{\text{elastic band}}| = \Delta \cdot dN/ds$. Since the the number of marks per distance travelled dN/ds decreases if we stretch the elastic band (and increases if we contract it), and Δ is a constant, this tangent vector is *not* normalized.

There is an energetic penalty associated with stretch and contraction. The scale of this energetic penalty is set by the *line tension* of the curve. In this work, we assume that the curve is not allowed to stretch at all.

2.3.1 Enforcing Normalization onto $\mathbf{T}(s)$

We have argued that the tangent vector $\mathbf{T}(s)$ is normalized. But how can we achieve this? We have considered several methods, each with their own advantages and disadvantages. A small list is shown below:

³We don't require the continuous analog: the Fourier transform. This is because the boundary conditions only allow for specific (discrete) modes. This can also be shown through a Fourier transform, of course.

⁴The coefficients must decrease *at least* faster than $1/k^5$ for the series to converge.

A Priori Normalization of $\mathbf{T}(s)$

If we write the tangent vector as

$$\begin{aligned}x'(s) &= \cos \psi(s), \\y'(s) &= \sin \psi(s),\end{aligned}$$

where $\psi(s)$ is the negative angle with the x -axis. Writing $\mathbf{T}(s)$ this way, we have *a priori* normalized the tangent vector. If we would like to use a method based on Fourier series, then there are basically two options:

1. Writing $\psi(s)$ as a Fourier series
2. Writing $x(s)$ as a Fourier series and computing $y'(s)$ from this or *vice versa*

In option 1 we are required to compute $x'(s), y'(s)$ from $\psi(s)$ since the energy is related to $x''(s), y''(s)$. The most obvious way of doing this is writing $\cos \psi(s)$ and $\sin \psi(s)$ as Taylor series:

$$\begin{aligned}\cos \psi(s) &= 1 - \frac{1}{2!} \psi(s)^2 + \frac{1}{4!} \psi(s)^4 - \frac{1}{6!} \psi(s)^6 + O(\psi(s)^7), \\ \sin \psi(s) &= \psi(s) - \frac{1}{3!} \psi(s)^3 + \frac{1}{7!} \psi(s)^7 + O(\psi(s)^8).\end{aligned}$$

Writing $x'(s), y'(s)$ as these Taylor series is allowed since $\psi(s)$ is bounded between 0 and π .⁵ Though this is in itself a quite elegant method, implementing the boundary conditions is no *walk in the park*: $x'(s)$ will be a polynomial of arbitrary degree in e^{iks} . Hence, enforcing the boundary conditions for $x(s), y(s)$ will involve a polynomial in the coefficients of the same degree. Solving the polynomial analytically is possible up to degree four, but past that it is only possible numerically, which is computationally very expensive if it has to be done every iteration step. Alongside this complication, it is desirable that the boundary conditions are satisfied *exactly*, which is not the case in this polynomial approximation.

Option 2 proposes that we write $x(s)$ as a Fourier series, and then writing $y'(s) = \sqrt{1 - x'(s)^2}$. We encountered one major problem with this approach though: $y'(s)$ can take on complex values. As soon as $x'(s) > 1$, $y'(s)$ will indeed be complex-valued. We also tried to put an energetic penalty on $y'(s)$ having an imaginary part, but this approach failed in some cases.

Including a Line Tension

One approach that is quite in line with the physics involved is to include a *line tension*. This energetic penalty might be represented in the following form:

$$\mathcal{E}_{\text{tension}} = \lambda \int ds \left(\mathbf{T}(s)^2 - 1 \right)^2,$$

which is always positive and real-valued. If we write $x'(s), y'(s)$ both as Fourier series, this energetic penalty will prohibit large deviations from normalization of $\mathbf{T}(s)$. For high values of λ we expect only small deviations from $\mathbf{T}(s)$ being normalized. We have not examined this method in this work.

⁵The fact that ψ is bounded is an assumption, but it is a very safe bet. The reason for this is that we are discussing systems that *resist bending*, and as such, we don't expect the shapes to have many knots. This assumption flies out the window if we would like to describe systems that will form many knots and twists, as is the case with protein folding, for example.

Constraining the Solution Set

The approach that we chose was simply constraining the solution set of $\mathbf{T}(s)$ to functions that satisfy $\mathbf{T}(s)^2 = 1$. Actually, we chose a slightly different path. We found that a statement like $\mathbf{T}(s)^2 = 1$ is difficult for a numerical solver to work with,⁶ so we chose $\mathbf{T}(s)^2 < 1 + \delta$, where δ is a small number. To further decrease the computational time, we selected a number of randomly selected coordinates $S = \{s_i\}$ in the interval $s \in [-\mathcal{A}/2, +\mathcal{A}/2]$, and only enforced the constraint $\mathbf{T}(s)^2 < 1 + \delta$ on those coordinates. In my Mathematica scripts I called this tolerance δT .

As soon as Mathematica found a critical solution, we checked whether the solution also satisfied a global arc-length constraint, as follows: $\int ds |\mathbf{T}(s)| = \mathcal{A} + \delta \mathcal{A}$, where $\delta \mathcal{A}$ is a small number.

2.4 Expansions of Bending Beams

The problem of curves that are subject to a bending energy can be described by various methods. By the way, let's just speak of "bending beams" from now on. The bending beam (in the small deformation limit) is often introduced in introductory classes to variational calculus. It is often represented as a differential equation, and in this small deformation limit it can be readily solved by analytical or numerical methods. Sadly, spine formation does not occur within the small deformation limit (quite the contrary, spines come in all sorts and varieties).

We will use an approach based on a Fourier series. There are several reasons why this method is suitable for our problem:

- A Fourier series probes the system of interest at *specific length scales*. Therefore the Fourier series has a direct and simple physical interpretation, related to these length scales.
- The energy functional that we are investigating is linear (i.e. it obeys the superposition principle). The energy functional will therefore be a simple function of the Fourier coefficients, as we shall see.
- The energy per term in the expansion is a rapidly increasing function of the wavenumber k . The energy landscape will therefore be dominated by the first few modes, such that we can make a cut-off at some value of the wavenumber. This is markedly different from a polynomial expansion in s , as we discussed in section 2.2.

Specifically, the (quasi-)Fourier expansion that we will be using can be written as

$$x(s) = \frac{\mathcal{L}}{\mathcal{A}}s + \sum_{k=-\infty}^{+\infty} \xi_k e^{iq_k s}, \quad (2.2)$$

$$y(s) = \sum_{k=-\infty}^{+\infty} \zeta_k e^{iq_k s}, \quad (2.3)$$

where the ξ_k, ζ_k are (complex) coefficients, q_k is the wavenumber of mode k and s is the arc-length traversed across the beam. The total arc-length traversed is denoted by \mathcal{A} . We call this a quasi-Fourier expansion because of the term $\mathcal{L}/\mathcal{A} \cdot s$, which is not usually present in Fourier expansions. This term won't make any difference for the energy functional, since its second-order derivative is zero.⁷ This

⁶The time that it took to solve the problem with an exact constraint and inexact constraint is at least ten times longer, and for some cases it was even found to be too long to monitor (over an hour for one set of parameters).

⁷Aside from the mathematics, it is clear from a more physical perspective why there should be no curvature energy associated with a linear term in s . A linear term in s defines the *direction* in which we are proceeding (left, right, up, under an 45° angle,...)–and we don't expect that the direction would matter for a bending energy, which experiences an energy due to a *change* in direction.

linear term is included because it allows us to easily implement the boundary conditions, as we will see in section 2.5.

We will choose a symmetric interval for s , such that $s \in [-\mathcal{A}/2, +\mathcal{A}/2]$.⁸

Now, the tangent vector $\mathbf{T}(s) = \{x'(s), y'(s)\}$ and its derivative $\mathbf{T}'(s) = \{x''(s), y''(s)\}$ are

$$\begin{aligned} x'(s) &= \frac{\mathcal{L}}{\mathcal{A}} + \sum_{k=-\infty}^{+\infty} \xi_k i q_k e^{iq_k s}, \\ y'(s) &= \sum_{k=-\infty}^{+\infty} \zeta_k i q_k e^{iq_k s}, \\ x''(s) &= - \sum_{k=-\infty}^{+\infty} \xi_k q_k^2 e^{iq_k s}, \\ y''(s) &= - \sum_{k=-\infty}^{+\infty} \zeta_k q_k^2 e^{iq_k s}. \end{aligned}$$

We will see in section 2.5 how the coefficients ξ_k, ζ_k relate to each other.

2.5 Implementation of Boundary Conditions and Constraints

The boundary conditions are relatively straightforwardly combined with the coefficients to the Fourier series.

Since $y'(s)$ is zero at $\pm\mathcal{A}/2$, we will write $y'(s)$ as a sine series (this corresponds to $y(s)$ being a cosine series). Similarly, since $x'(s)$ is unity at $\pm\mathcal{A}/2$, we will write $x'(s)$ as a cosine series (this corresponds to $x(s)$ being a sine series).⁹ Furthermore, since the values of $x(s), y(s)$ are stationary at $\pm\mathcal{A}/2$, we require that only wavenumbers are allowed that are stationary at these coordinates. This property is fulfilled by wavenumbers $q_k = 2k\pi/\mathcal{A}$ where k is an integer.

Combining the allowed wavenumbers $q_k = 2k\pi/\mathcal{A}$ with the fact that $x(s)$ can be written as a sine series and $y(s)$ as a cosine series, we have

$$\begin{aligned} x(s) &= \frac{\mathcal{L}}{\mathcal{A}} s + \sum_{k=1}^n \alpha_k \sin\left(\frac{2\pi k s}{\mathcal{A}}\right), \\ y(s) &= \beta_0 + \sum_{k=1}^n \beta_k \cos\left(\frac{2\pi k s}{\mathcal{A}}\right), \end{aligned}$$

where α_k, β_k are real-valued coefficients. If we now substitute $y(\mathcal{A}/2) = 0$ we find $0 = \beta_0 + \sum_k (-1)^k \beta_k$, or

$$\beta_0 = - \sum_{k=1}^n (-1)^k \beta_k.$$

Since $y'(0) = y'(\pm\mathcal{A}/2) = 0$ we have $x'(0) = x'(\pm\mathcal{A}/2) = 1$. We have, therefore, the following

⁸Which is a little different from the more customary way of writing $s \in [0, \mathcal{A}]$, but that is entirely equivalent to the definition in this work, of course.

⁹Remember that $x(s)$ actually was a *quasi-Fourier* series due to a linear term in s .

equations:

$$\begin{aligned} 1 &= \frac{\mathcal{L}}{\mathcal{A}} + \frac{2\pi}{\mathcal{A}} \sum_{k=1}^n k\alpha_k (-1)^k, \\ 1 &= \frac{\mathcal{L}}{\mathcal{A}} + \frac{2\pi}{\mathcal{A}} \sum_{k=1}^n k\alpha_k, \end{aligned}$$

which are readily solved by:

$$\begin{aligned} \alpha_1 &= - \sum_{k=3, k \text{ odd}}^n k\alpha_k, \\ \alpha_2 &= \frac{\mathcal{A} - \mathcal{L}}{4\pi} - \frac{1}{2} \sum_{k=4, k \text{ even}}^n k\alpha_k. \end{aligned}$$

To summarize: In this section we have incorporated the boundary conditions—as presented in equations (1.2) and displayed in figure 1.2—in a Fourier expansion. This Fourier expansion satisfies the boundary conditions, but it's bending energy isn't minimized. For that, we require the program as explained in appendix A. The energy we will be minimizing is computed analytically below in section 2.6.

2.6 Energy of Fourier Expansion

Since the wavenumbers are discrete values $2k\pi/\mathcal{A}$ on an interval of length \mathcal{A} , the various modes are orthogonal. This property is of great use to us, because the energy can now be easily expressed as a sum over coefficients. The energy functional is:

$$\begin{aligned} \mathcal{E}/K_b &= \int_{-\mathcal{A}/2}^{+\mathcal{A}/2} ds \left(x''(s)^2 + y''(s)^2 \right) \\ &= \int_{-\mathcal{A}/2}^{+\mathcal{A}/2} ds \left(\sum_{k=1}^n \alpha_k \left(\frac{2\pi k}{\mathcal{A}} \right)^2 \sin \left(\frac{2\pi ks}{\mathcal{A}} \right) \right)^2 + \left(\sum_{k=1}^n \beta_k \left(\frac{2\pi k}{\mathcal{A}} \right)^2 \cos \left(\frac{2\pi ks}{\mathcal{A}} \right) \right)^2, \end{aligned}$$

where all integrals with different wavenumbers are zero, and those with the same wavenumber have $\int ds (\sin q_k s)^2 = \int ds (\cos q_k s)^2 = \mathcal{A}/2$. We have, therefore, the following result for the energy:

$$\mathcal{E}/K_b = \frac{8\pi^4}{\mathcal{A}^3} \sum_{k=1}^n k^4 (\alpha_k^2 + \beta_k^2).$$

A simple dimensional analysis reveals some of the scaling behavior of \mathcal{E}/K_b : Since the α_k, β_k have dimensions of length, \mathcal{E}/K_b will have dimensions of 1/length. What does this mean? Well, it means that a curve that resists bending would like to grow, *ad infinitum*. Since the totally relaxed state ($\mathcal{A} = \mathcal{L}$) is the energetically most favorable, we expect there is a critical arc-length \mathcal{A}^* for which the energy is maximal. For $\mathcal{A} < \mathcal{A}^*$ the system wants to relax to its ground state, but for $\mathcal{A} > \mathcal{A}^*$ the system spontaneously grows.

Chapter 3

Results

This part of the monograph summarizes the results that we have found on the bending of curves. With “results” I am referring to the shapes that we have found, some analysis of these shapes, but also the stability and convergence of the minimization algorithm that we have used.

3.1 Shapes

We have modeled morphology of one-dimensional shapes under influence of the Canham-Helfrich functional (2.1). We did this using *increments* in the arc-length. That is to say, we started with a shape that has $\mathcal{A} \gtrsim \mathcal{L}$ and increased \mathcal{A} with small increments. At each point in this sequence of arc-lengths, we used the previous solution as an initial guess to the solver. This is similar in spirit to a ‘physical’ growth process.¹

Below, in figures 3.2 and 3.3, we have shown a subset of the evolution of shapes. I feel that this behavior is quite in line with my physical intuition.² There are several interesting morphological aspects in these shapes. For one, there is clear formation of a large head for $\mathcal{A} \gtrsim 2.75$. At the same time, there is a thinning neck. In particular, for $\mathcal{A} \approx 6.50$ the neck width has become approximately zero. The shapes with a large head and small neck might be called ‘balloons’, for two reasons: i) Superficially, the shapes look like balloons, ii) The energy *decreases* with increasing size (as we will see in section 3.2.1), similar to inflation of a balloon.

Another interesting feature is that there is, as predicted in section 2.6, a maximum energy at a critical arc-length \mathcal{A}^* . From the images we can see that $\mathcal{A}^* \approx 2.25$. More accurate estimation of the critical arc-length gives approximately the same number ($\mathcal{A}^* \approx 2.17$), as we shall see shortly.



Figure 3.1: Departure of Jacques Charles and Marie-Noel Robert’s ‘aerostatic globe’ balloon from the Jardin des Tuileries, Paris, on Dec. 1, 1783.

¹Various mechanisms are known that cause growth (or, at least, correlate with growth), such as: exocytosis [21; 15] and growth of actin [24; 14; 2].

²Except for the shapes with $\mathcal{A} \approx 8 - 10$ —I expected to see *circular* shapes, not the ‘lemniscate’ shapes which are visible for $\mathcal{A} \approx 8 - 10$. Since it is to be expected that there is a crossover from balloon morphology (for $\mathcal{A} \approx 4 - 6.50$) to lemniscate morphology, it is *not* counter intuitive that there *are* lemniscate morphologies—it is counter intuitive that these are the *only* shapes that we were able to find. In fact, I expected (as did Kees Storm), that the circular shapes (which we couldn’t find) would be lower in energy. However, these findings do not exclude the circular shapes for $\mathcal{A} > 10$.

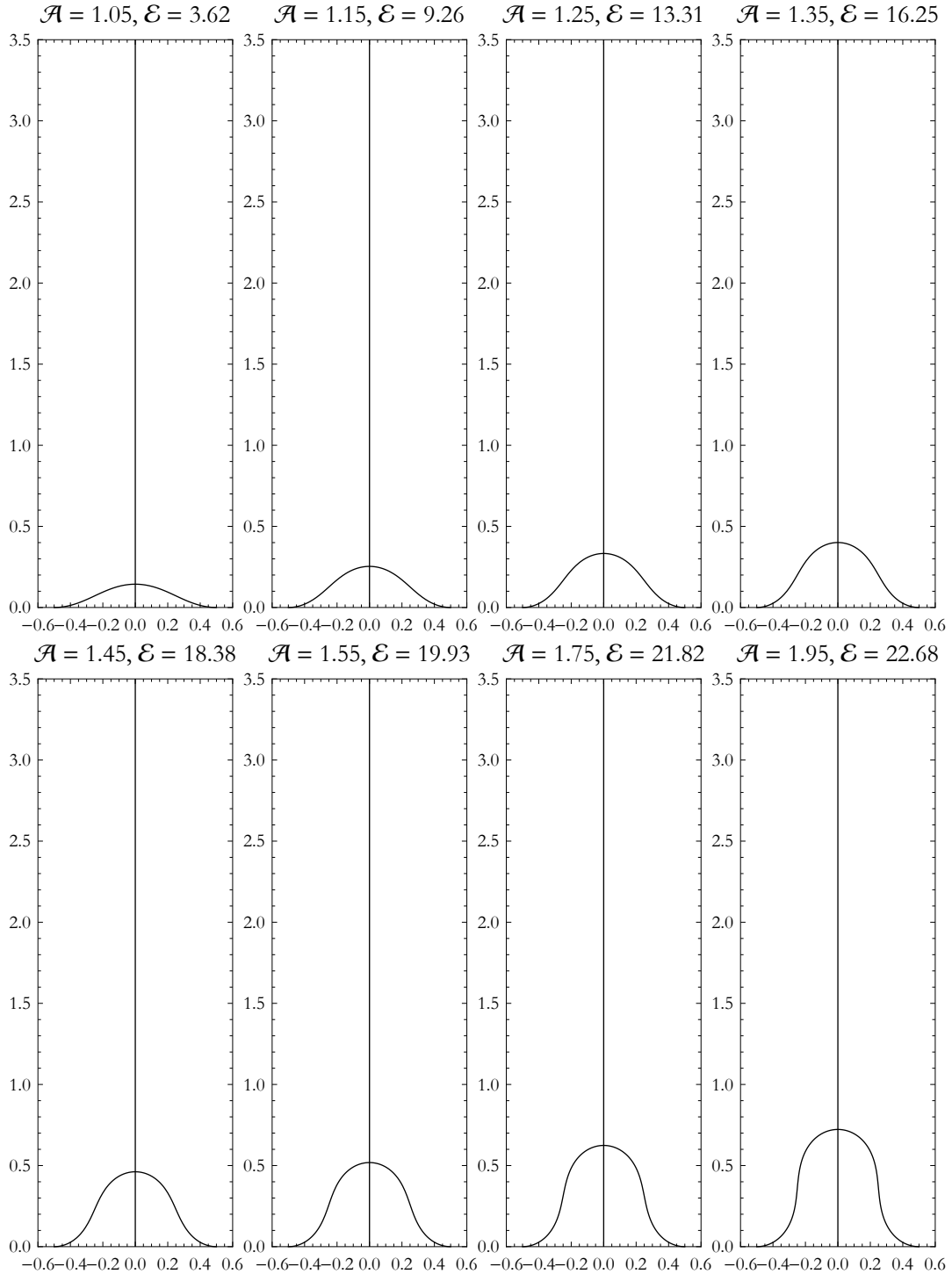


Figure 3.2: Shapes for various arc-lengths. The arc-length \mathcal{A} and energy \mathcal{E} are indicated in the figures. The tolerance in tangent normalization is $\delta T = 0.1\%$, the tolerance in the total arc-length constraint is $\delta\mathcal{A} = 0.5\%$ and the number of Fourier modes is $n = 10$.

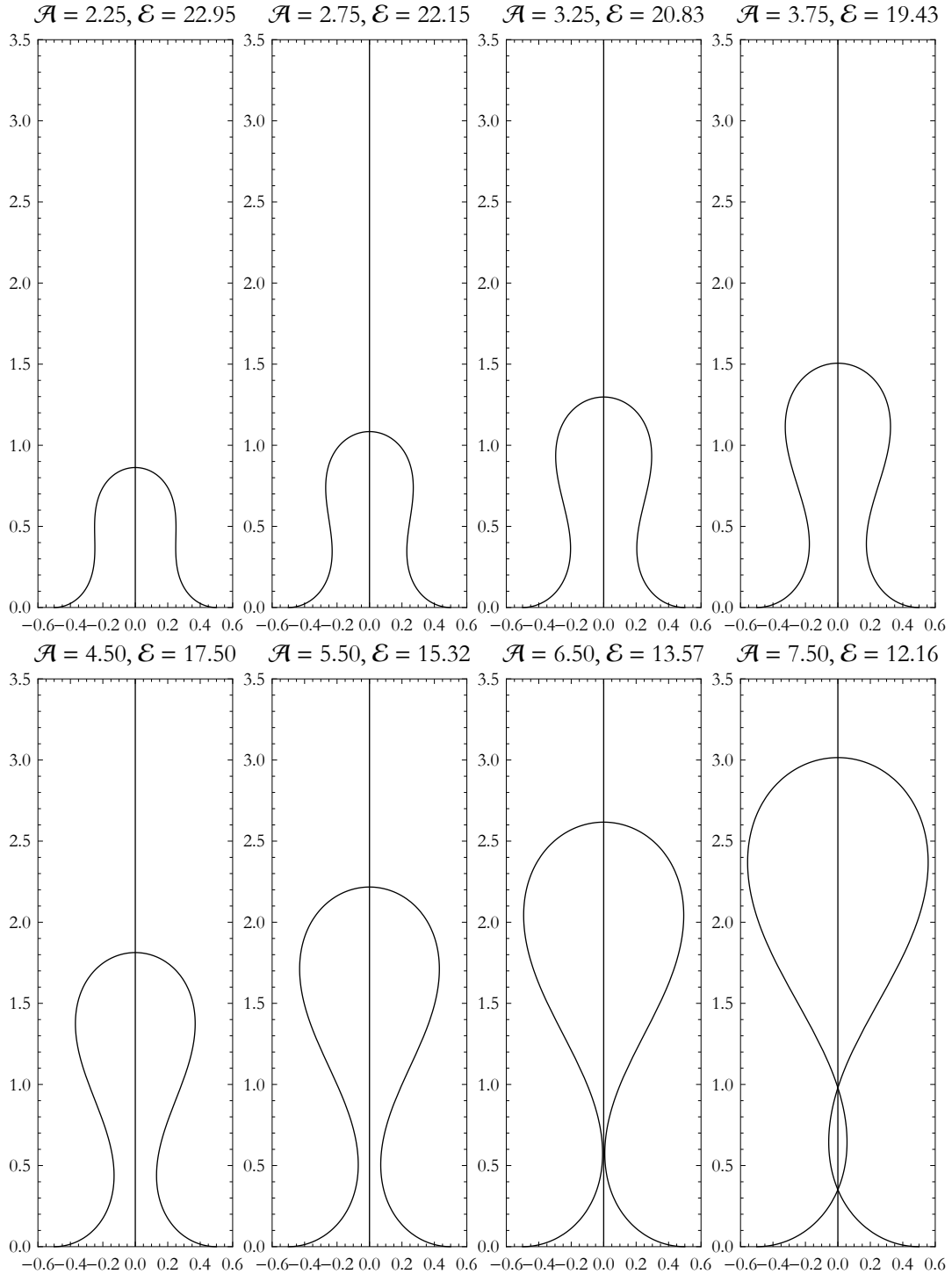


Figure 3.3: Shapes for various arc-lengths. The arc-length \mathcal{A} and energy \mathcal{E} are indicated in the figures. The tolerance in tangent normalization is $\delta T = 0.1\%$, the tolerance in the total arc-length constraint is $\delta \mathcal{A} = 0.5\%$ and the number of Fourier modes is $n = 10$.

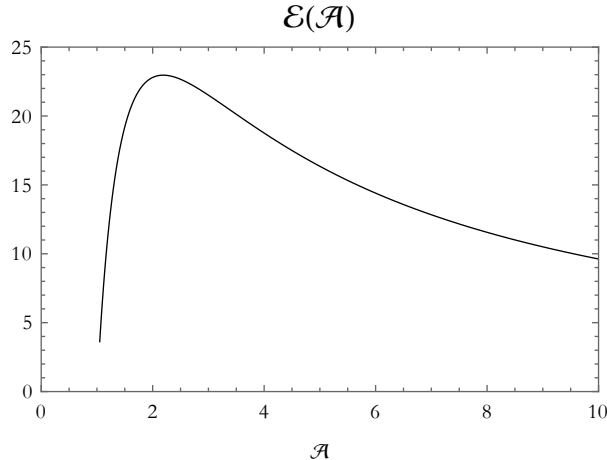


Figure 3.4: The total energy of the shape \mathcal{E} (in units of K_b/\mathcal{L}) versus it's total arc-length (in units of \mathcal{L}).

3.2 Quantitative Analysis of Shape Morphology

In the previous section I have qualitatively discussed some of the features of the shape morphology. In this section, I will define some (quantitative) metrics and show the scaling behavior of these metrics with respect \mathcal{A} . These metrics are: The total energy \mathcal{E} , the “power spectral density” $\{\mathcal{E}_k\}$ (which is simply the energy per Fourier mode), some analysis of the size of the shapes, and—last but not least—a toy model for shape growth.

3.2.1 Energy Landscape of Shape Growth

The energy landscape $\mathcal{E}(\mathcal{A})$ is quite easy to understand. In the fully relaxed state $\mathcal{A} = \mathcal{L}$ the energy is identically zero, and for $\mathcal{A} \gg 1$ the scaling of \mathcal{E} dictates that $\mathcal{E} \sim 1/\mathcal{A}$ —which is a decreasing function of \mathcal{A} . We therefore expect that there is a critical arc-length \mathcal{A}^* . This prediction bears out if we plot the energy landscape $\mathcal{E}(\mathcal{A})$. This energy landscape is shown in figure 3.4. This plot tells us that $\mathcal{A}^* \approx 2.2$.

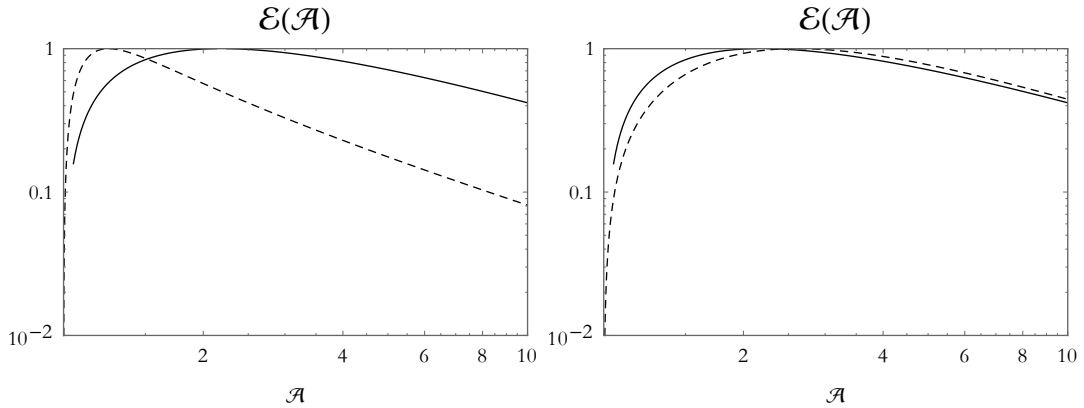
I have produced a cute scaling argument that predicts an estimate for the critical arc-length. To this end, let's work in a Monge representation $y = y(x)$ with only one mode:

$$y(x) \equiv \beta_0 + \beta_1 \cos \frac{2\pi x}{\mathcal{L}},$$

which is the lowest mode possible in an interval $x = -\mathcal{L}/2, +\mathcal{L}/2$. We have the boundary conditions $y(\pm\mathcal{L}/2) = 0$, which corresponds to $\beta_0 = \beta_1 \equiv \beta$. The squared curvature is

$$\begin{aligned} H^2 &= \frac{y''(x)^2}{(1 + y'(x)^2)^3} \\ &\sim \frac{\beta^2 \left(\frac{2\pi}{\mathcal{L}}\right)^4}{1 + \beta^2 \left(\frac{2\pi}{\mathcal{L}}\right)^2 + \beta^4 \left(\frac{2\pi}{\mathcal{L}}\right)^4}, \end{aligned}$$

where I kept up to fourth order in $1/\mathcal{L}^4$ and removed factors of order unity. Let's make matters easier



(a) Plots of the normalized energy landscape $\mathcal{E}/\mathcal{E}_{\max}$ (—) and(b) Plots of the normalized energy landscape $\mathcal{E}/\mathcal{E}_{\max}$ (—) and the toy-model $\mathcal{E} \sim x/(1+x+x^2)$ (---).
the toy-model fitted to the ‘measured’ result $\mathcal{E} \sim 0.155x/(1+0.155x+(0.155x)^2)$ (---).

Figure 3.5: Plots of the normalized energy landscape $\mathcal{E}/\mathcal{E}_{\max}$ (—) and the toy-model (---) proposed in this section versus arc-length \mathcal{A} . These plots have been graphed on logarithmic scales to more clearly show the different scaling regimes.

by writing $2\pi\beta/\mathcal{L} \equiv \tilde{\beta}$, to find:

$$H^2 \sim \left(\frac{2\pi}{\mathcal{L}}\right)^2 \frac{\tilde{\beta}^2}{1 + \tilde{\beta}^2 + \tilde{\beta}^4}.$$

Now, area normalization requires

$$\begin{aligned} \mathcal{A} &= \int dx \sqrt{1 + y'(x)^2} \\ &\sim \mathcal{L} \left(1 + \frac{1}{4}\tilde{\beta}^2 - \frac{3}{16}\tilde{\beta}^4\right), \end{aligned}$$

from which we find $\tilde{\beta}^2 = \frac{2}{3} \pm \frac{2}{3}\sqrt{13 - 12\mathcal{A}/\mathcal{L}}$ of which we require the minus sign since $\mathcal{A}/\mathcal{L} = 1$ should correspond to $\tilde{\beta} = 0$. Hence, we have $\tilde{\beta}^2 = \frac{2}{3}(1 - \sqrt{13 - 12\mathcal{A}/\mathcal{L}})$. A series expansion of this formula is $\tilde{\beta}^2 \sim 4(\tilde{\mathcal{A}} - 1)$, where $\tilde{\mathcal{A}} = \mathcal{A}/\mathcal{L}$ is the reduced arc-length. If we substitute this expression for $\tilde{\beta}$ in the squared curvature, we find:

$$H^2 \sim \left(\frac{2\pi}{\mathcal{L}}\right)^2 \frac{4(\tilde{\mathcal{A}} - 1)}{1 + 4(\tilde{\mathcal{A}} - 1) + (4(\tilde{\mathcal{A}} - 1))^2},$$

or,

$$\mathcal{E}/K_b \sim \frac{4\pi^2}{\mathcal{L}} \frac{x}{1 + x + x^2},$$

where $x \equiv 4(\tilde{\mathcal{A}} - 1)$. We can plot this function versus x (as I have done in figure 3.5a) to observe a clear maximum at $x^* = 1$, or $\tilde{\mathcal{A}}^* = 1 + x^* = 1.25$. This value is not very close to the ‘measured’ critical arc-length of 2.2, which is to be expected since we put several factors to unity. The scaling of this toy-model appears to be correct: There is the expected linear scaling for small $\mathcal{A} \approx \mathcal{L}$ and the expression scales like $1/\mathcal{L}x \sim 1/\mathcal{A}$ for $\mathcal{A} \gg \mathcal{L}$.

The general behavior of this toy model and the measured result is similar, but not entirely equivalent. Well, it would have been quite surprising if it *were* equivalent, since we set some factors of order unity *equal* to unity. In particular, the number four in $x \equiv 4(\mathcal{A} - 1)$ was found by an approximation. If we now modify this number to 0.155×4 , we find much better agreement, as is clear from figure 3.5b. In particular, the scaling and position of the maximum of the ‘measured’ result and toy model are similar. These similarities suggest that the scaling argument $\mathcal{E} \sim \mathcal{A}^{-1}$ for large \mathcal{A} is indeed correct.

3.2.2 The Power Spectral Density—Which Length-Scales Matter?

The total energy of the curve has been written as

$$\mathcal{E}/K_b = \frac{8\pi^4}{\mathcal{A}^3} \sum_{k=1}^n k^4 (\alpha_k^2 + \beta_k^2).$$

From this expression, the power spectral density (or energy per mode) can be computed in a very straightforward manner, since this energy is a sum over each distinct mode. We therefore assert that the energy ‘contained in one mode’ is

$$\mathcal{E}_k = \frac{8\pi^4}{\mathcal{A}^3} k^4 (\alpha_k^2 + \beta_k^2).$$

The function \mathcal{E}_k shows a clear pattern. In figure 3.6 we have shown it for various values of the total arc-length. In particular, there appears to be a *linear regime* on these logarithmic scales, corresponding to \mathcal{E}_k being an exponential function of k . This, then, corresponds to \mathcal{E}_k having a *typical length-scale* depending on the slope of the linear part of the logarithmic plot. Alongside this linear regime, there is a *plateau regime* for small k . This is particularly clear for large values of \mathcal{A} . This means that these values of k (in the plateau regime) share approximately the same energy. It is not clear to us why the energy spectrum increases for large values of k , but we can safely ignore this peculiarity since the energy scale in this regime only affects $< 0.01\%$ of the total energy. This plateau regime is analyzed in more detail in appendix B on page 39.

Let’s say that the linear regime is denoted $\mathcal{E}_k = \hat{\mathcal{E}}_k \cdot e^{-k/\kappa}$ with κ the *typical number of modes* and $\lambda = \mathcal{A}/\kappa$ the *typical length-scale*.³ The typical number of modes tells us how many or how few modes have to be taken into account to describe the energy landscape. For some value κ , only the modes up to κ contribute to the energy landscape. *Vice versa*, the modes $k \gg \kappa$ can be neglected. I don’t think that it is trivial that there *is* such a typical number of modes—think, for instance, of the equipartition of energy, in which *all* modes contribute equally to the energy landscape.⁴ Luckily, however, we have the luxury of being able to cut-off the Fourier series at, say, $n = 5\kappa$.⁵

We can estimate the typical mode most directly by plotting $\log(\mathcal{E}_k/\hat{\mathcal{E}}_k) = -k/\kappa$ and estimating the slope $-1/\kappa$. This function is visualized in figure 3.7.

But before we measure these slopes, can we “guess” what typical length-scales are associated with these shapes? For $\mathcal{A} \approx \mathcal{L}$ we would expect that the typical length-scale is somewhat smaller than, but in the order of \mathcal{L} . Since the definition of κ is that the $k > \kappa$ are immaterial, we might say that any length-scale smaller than \mathcal{L}/κ is immaterial.

Conversely, for $\mathcal{A} \gg \mathcal{L}$ we would expect that κ is independent of \mathcal{L} . In fact, we expect that the only length-scale present is \mathcal{A} itself—since there is no other length-scale in the system to choose from.

³This relation can be found as follows: One Fourier mode is e^{iqs} with q the wavenumber. In our case, $q = 2\pi ks/\mathcal{A}$, so the typical length-scale of mode k is \mathcal{A}/k .

⁴Equipartition of energy refers to deviations from equilibrium. We are not describing an equilibrium situation (except for the cases $\mathcal{A} = \mathcal{L}$ and $\mathcal{A} \rightarrow \infty$, which we don’t consider), so this is a whole different story—but this example was simply chosen to illustrate the point that I am trying to make here.

⁵Since the energy landscape is approximately exponential with respect to k , the term with $k = 5\kappa$ contributes only $e^{-5} \approx 7\%$.

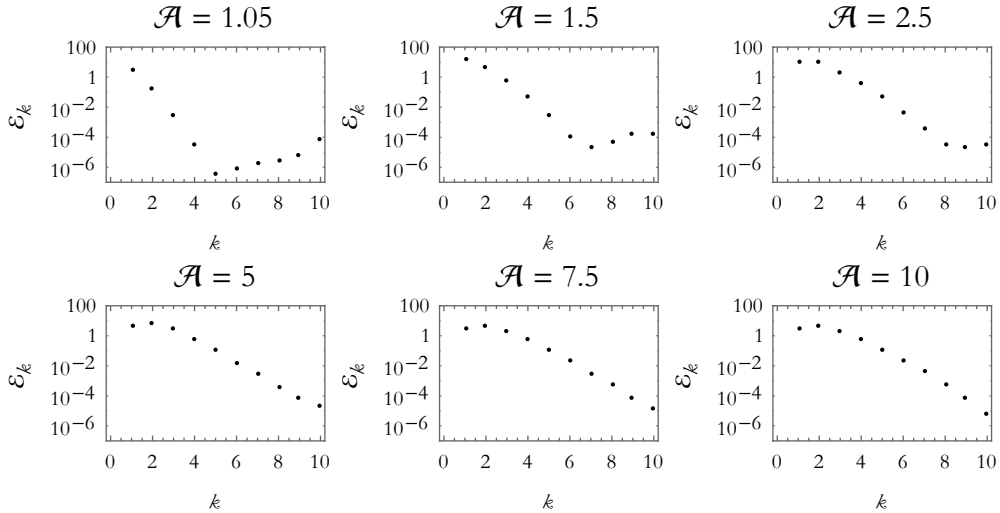


Figure 3.6: Power spectral densities \mathcal{E}_k for various arc-lengths and wavenumbers $k = 0 \dots 10$. The energy corresponding to $k = 0$ is identically zero. These power spectral densities have been computed by an average over 10 identical runs of the program, with the tolerance in the arc-length $\delta\mathcal{A} = 0.5\%$ and a normalization tolerance $\delta T = 0.1\%$.

This prediction should bear out by having a λ that is proportional to \mathcal{A} , or, equivalently, a κ being independent of \mathcal{A} .

Below, in table 3.1 I have catalogued the (negative) slopes $1/\kappa$ and the typical length-scales λ derived from this. We observe that our predictions indeed bear out: The typical length-scale for $\mathcal{A} \approx \mathcal{L}$ is a somewhat smaller value than \mathcal{L} , and for $\mathcal{A} \gg \mathcal{L}$ it is about 50% of \mathcal{A} . Also, it is quite clear that the typical number of modes κ is independent of \mathcal{A} for $\mathcal{A} \gg \mathcal{L}$.

Table 3.1: The typical width $1/\kappa$ of the energy spectrum, and the typical length-scales $\lambda = \mathcal{A}/\kappa$ for different values of the total arc-length.

\mathcal{A}	Slope $1/\kappa$	Typical reduced length-scale λ/\mathcal{L}
1.05	4.4–4.5	0.23–0.24
1.5	2.6–3.2	0.47–0.58
2.5	2.1–2.7	0.93–1.19
5.	1.7–2.0	2.50–2.94
7.5	1.7–1.9	3.95–4.41
10.	1.7–1.9	5.26–5.88

What does this section tell us? Well, the title reveals the content, in this case. We have made plausibly by examining the power spectral density—that only a *limited* set of length-scales matter for the shapes that we are investigating. To be precise about it, the energy per mode \mathcal{E}_k is exponentially decaying with respect to k , and therefore we can infer that it is allowed to cut-off all higher order modes above some critical mode number κ . We have estimated this number of modes κ by examining the slope of the power spectral density, and found that 10 modes (*viz.* the number of modes that we have used in our computations) is more than sufficient. This can be verified quite easily by examining the astronomically small energies per mode \mathcal{E}_k for $k \gtrsim 6$ (shown in figure 3.7).

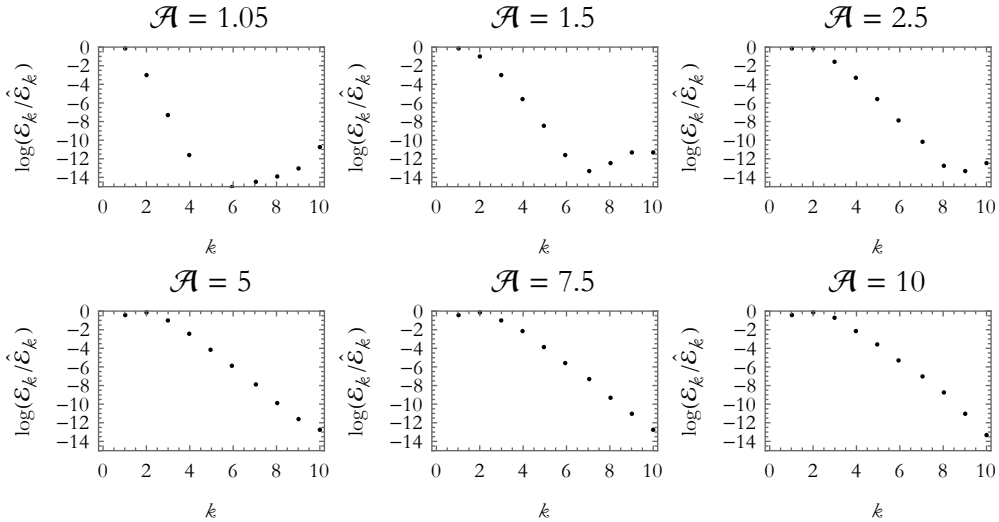


Figure 3.7: Logarithm of the normalized power spectral densities $\log(\mathcal{E}_k/\hat{\mathcal{E}}_k)$ for various arc-lengths and wavenumbers $k = 0 \dots 10$. These power spectral densities have been computed by an average over 10 identical runs of the program, with the tolerance in the arc-length $\delta\mathcal{A} = 0.5\%$ and a normalization tolerance $\delta T = 0.1\%$.

3.2.3 Shape Height, Head and Neck Width

In this part of the monograph, we will examine some quantitative metrics of the morphology: Shape height, head width and neck width. Shape height is a well-defined quantity for the shapes that we examined, but a head (and, consequently, a neck) was only observed for $\mathcal{A} \gtrsim 2.25$.

Shape Height

Since the curve is a one-dimensional structure, we expect that the distance between two points on the curve increases (approximately) linearly with \mathcal{A} . This argument can be made more exact as follows: The normalization criterion is $1 = x'(s)^2 + y'(s)^2 = \frac{\mathcal{L}}{\mathcal{A}} + \sum_k \left(\frac{2\pi k}{\mathcal{A}} \right)^2 (\alpha_k^2 + \beta_k^2)$. The last term in this expression can be neglected for $\mathcal{A} \gg \mathcal{L}$, so we observe that—in order for the terms to be of order unity—the α_k, β_k must scale proportional to \mathcal{A} . The shape height, then, is $y(0) = \sum_{k \text{ odd}} 2\beta_k \sim \mathcal{A}$. We can get an estimate of the coefficient in this linear relationship $y(0) = \eta\mathcal{A}$ if we suppose that the shape is approximately semicircular (which is an extremely crude approximation). Within this approximation we have $\eta = \pi^{-1} \approx 0.32$.

The results tell us what we expected: A linear relationship between $y(0)$ and \mathcal{A} . The results have been plotted in figure 3.8. The prediction using a semicircular shape with $y(0) \approx 0.32\mathcal{A}$ is surprisingly close to the fit to the ‘measured’ values $y(0) = 0.4017\mathcal{A}$.

Head and Neck Diameter

Similar to the shape height, we expect that the head and neck diameter will increase linearly with \mathcal{A} . We observe that from $\mathcal{A} = 2.25 \equiv \mathcal{A}_{\text{neck}}$ there is formation of a head, and that the neck obtains a width of zero at $\mathcal{A} = 6.60 \equiv \mathcal{A}_{\text{cross}}$. At the point where there is the first sign of a head, the neck is located at the coordinate $(\frac{1}{2}, \frac{1}{2})$, and it seems that at the first point of self-crossing the width of the neck is unity.

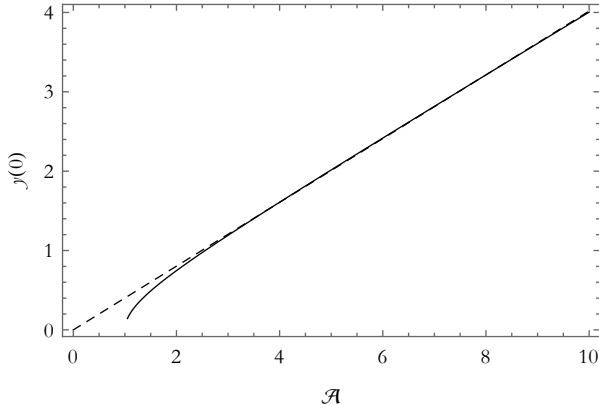


Figure 3.8: The height of the shape $y(0)$ versus the arc-length \mathcal{A} (both in units of \mathcal{L}). The linear ‘fit’ is $y(0) = 0.4017 \cdot \mathcal{A}$.

Hence, we are able to write the following toy-models for the head and neck diameters:

$$\begin{aligned} d_{\text{neck}} &= \frac{1}{2} - \frac{1}{2} \frac{\mathcal{A} - \mathcal{A}_{\text{neck}}}{\mathcal{A}_{\text{cross}} - \mathcal{A}_{\text{neck}}}, \\ d_{\text{head}} &= \frac{1}{2} + \frac{1}{2} \frac{\mathcal{A} - \mathcal{A}_{\text{neck}}}{\mathcal{A}_{\text{cross}} - \mathcal{A}_{\text{neck}}}, \end{aligned}$$

such that the ratio between the two is:

$$\frac{d_{\text{head}}}{d_{\text{neck}}} = \frac{\Delta \mathcal{A} + (\mathcal{A} - \mathcal{A}_{\text{neck}})}{\Delta \mathcal{A} - (\mathcal{A} - \mathcal{A}_{\text{neck}})},$$

where $\Delta \mathcal{A} \equiv \mathcal{A}_{\text{cross}} - \mathcal{A}_{\text{neck}}$. For \mathcal{A} close to $\mathcal{A}_{\text{neck}}$ this ratio is approximately unity, but close to $\mathcal{A}_{\text{cross}}$ it diverges as $1/(\mathcal{A}_{\text{cross}} - \mathcal{A})$. This toy-model is in excellent agreement with the ‘measured’ result, as is clearly visible in figure 3.9.

3.2.4 Shape Volume

We define the two-dimensional volume (i.e. the area under the curve) as follows:

$$\begin{aligned} \mathcal{V} &\equiv \int |dy| x \\ &= \int_{-\mathcal{A}/2}^{+\mathcal{A}/2} ds |x(s)y'(s)|. \end{aligned}$$

This function is readily graphed for various values of \mathcal{A} . We have shown the data in figure 3.10a. For large \mathcal{A} , we expect the shape volume to scale like \mathcal{A}^2 . For $\mathcal{A} \approx \mathcal{L}$ the shape volume will be approximately $\frac{1}{2}\mathcal{L} \cdot h$ where h is the height of the shape, with $h \approx \frac{1}{2}\sqrt{\mathcal{A}^2 - \mathcal{L}^2} \approx \frac{1}{\sqrt{2}}\sqrt{\mathcal{L}}\sqrt{\mathcal{A} - \mathcal{L}}$ so $\mathcal{V} \approx \frac{1}{2}\mathcal{L}^{3/2}\sqrt{\mathcal{A} - \mathcal{L}}$. For intermediate values there will, therefore, likely be some transition regime.

The different scaling regimes of \mathcal{V} can be determined by plotting $\log(\mathcal{V}/\mathcal{L}^2)$ versus $\log(\mathcal{A}/\mathcal{L} - 1)$, which has been done in figure 3.10b. This plot reveals that there is scaling—as predicted—like $\sim (\mathcal{A} - \mathcal{L})^{1/2}$ for $\mathcal{A} \approx \mathcal{L}$, and $\sim \mathcal{A}^2$ for $\mathcal{A} \gg \mathcal{L}$.

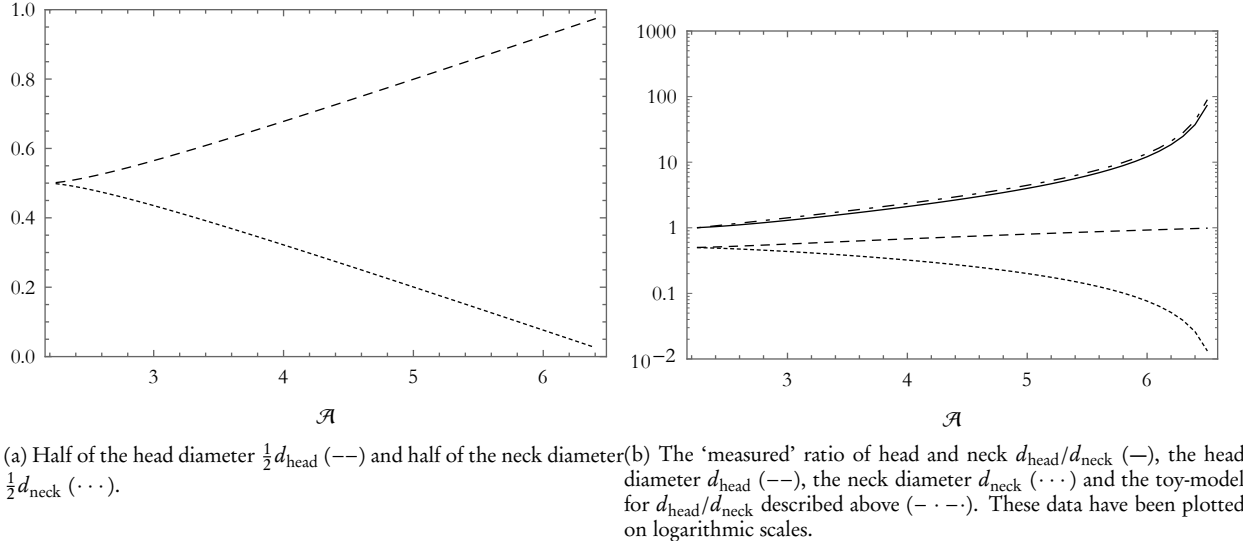


Figure 3.9: Left: The ‘measured’ values of d_{neck} , d_{head} . These data were graphed here to display the linear relationship between d_{neck} , d_{head} and \mathcal{A} . Right: There is excellent agreement between the ‘measured’ ratio of head and neck diameter and the toy-model.

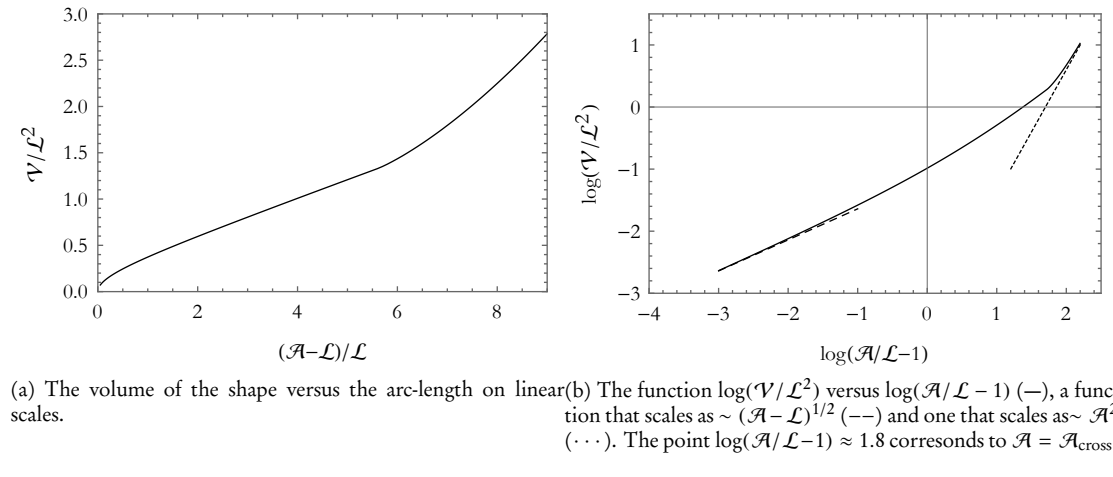


Figure 3.10: Left: The volume of the shape versus the arc-length on linear scales. Right: The function $\log(\mathcal{V}/\mathcal{L}^2)$ versus $\log(\mathcal{A}/\mathcal{L}-1)$ with two distinct scaling regimes.

3.3 Dynamics of Shape Growth

One of the more pregnant questions that arise if we look at figure 3.4 is:

“How will the shape evolve if we *release* the shape at some particular value of the arc-length \mathcal{A}_0 ?”

Because we have completely ignored time-dependent processes, this question cannot be answered with the theory and results that we have shown up to this point. To counteract that deficiency, we will

present models in this section to analyze the *dynamics* of shape growth. How the shape $\mathcal{A}(t)$ will evolve will not only depend on the minimal energy under any given arc-length—which is what we have already discussed—but also on *how we get there*. Well, how do we get “there”, then? Unfortunately (or fortunately?), there are a *kazillion* ways to get from \mathcal{A}_0 to $\mathcal{A}(\infty) \equiv \mathcal{A}_\infty$. This is the point where taste and creativity enter our work. We chose to discuss three simple models. We present them in the following order:

- Section 3.3.1 Dynamics of shape growth due to the potential landscape $d_{\mathcal{A}}\mathcal{E}$
- Section 3.3.2 Dynamics due to $d_{\mathcal{A}}\mathcal{E}$ beforementioned, but including a *growth term* that scales as $\sim \mathcal{A}$.
- Section 3.3.3 Dynamics due to $d_{\mathcal{A}}\mathcal{E}$ beforementioned, but including a growth term that scales as $\sim \mathcal{A}$ and a *growth inhibition term* that scales as $\sim 1/d_{\text{neck}}$.

3.3.1 Dynamics Due to a Potential Landscape

Without doing any difficult mathematics, we can qualitatively understand the shape evolution in a potential landscape $\mathcal{E}(\mathcal{A})$ (this potential landscape is shown in figure 3.4). To begin with, if the energy $\mathcal{E}(\mathcal{A})$ is located at a critical point, we expect that \mathcal{A} will be constant in time. In our case, we have argued in section 3.2.1 that there are two such critical points: The totally relaxed state $\mathcal{A} = \mathcal{L}$ and the critical arc-length $\mathcal{A}^* \approx 2.2$. Furthermore, we expect that the shape will always tend to evolve towards the state of lowest energy—and hence, the variation in arc-length will change accordingly. We can hypothesize a simple model that emulates these dynamics:

$$\begin{aligned}\frac{d\mathcal{A}}{dt} &= -g \frac{d\mathcal{E}}{d\mathcal{A}}, \\ \mathcal{A}(0) &= \mathcal{A}_0,\end{aligned}$$

where $g > 0$ is a *dynamical constant* that tells us how fast the shape grows (or shrinks) in reaction to a nearby valley (or bump) in the energy landscape $\mathcal{E}(\mathcal{A})$. Since $\mathcal{E}(\mathcal{A})$ is known, this first-order differential equation can be readily be solved by numerical methods.

The constant g has dimensions of length²/(energy × time). From now on, we will not use t as the independent variable, but rather the dimensionless time $\tilde{t} \equiv gK_b t / \mathcal{L}^3$. Using solely reduced quantities, we have the dynamical equation

$$\frac{d\tilde{\mathcal{A}}}{d\tilde{t}} = -\frac{d\tilde{\mathcal{E}}}{d\tilde{\mathcal{A}}},$$

where $\tilde{\mathcal{A}} \equiv \mathcal{A}/\mathcal{L}$ is the reduced arc-length and $\tilde{\mathcal{E}} \equiv \mathcal{L}\mathcal{E}/K_b$ is the reduced energy.

We solved this differential equation by making a least-squares fit to the data $d\tilde{\mathcal{E}}/d\tilde{\mathcal{A}}$.⁶ Then, Mathematica is able to use numerical routines to solve the differential equation. In figure 3.11 we have shown the results of this experiment. We observe that the critical arc-length \mathcal{A}^* corresponds to an unstable equilibrium, since a small deviation from \mathcal{A}^* corresponds to a substantially different shape evolution $\mathcal{A}(t)$. This is to be expected, since the critical arc-length \mathcal{A}^* corresponds to a *maximum* in the energy landscape. Any value $\mathcal{A}_0 > \mathcal{A}^*$ will enable the shape to *grow*, and $\mathcal{A}_0 < \mathcal{A}^*$ will have the shape *relax* towards its totally relaxed state ($\mathcal{A} = \mathcal{L}$).

⁶We used a polynomial in $1/\mathcal{A}$ since these terms converge to zero for $\mathcal{A} \gg \mathcal{L}$. Moreover, this polynomial gives the correct scaling $\mathcal{E} \sim 1/\mathcal{A}$ for $\mathcal{A} \gg \mathcal{L}$.

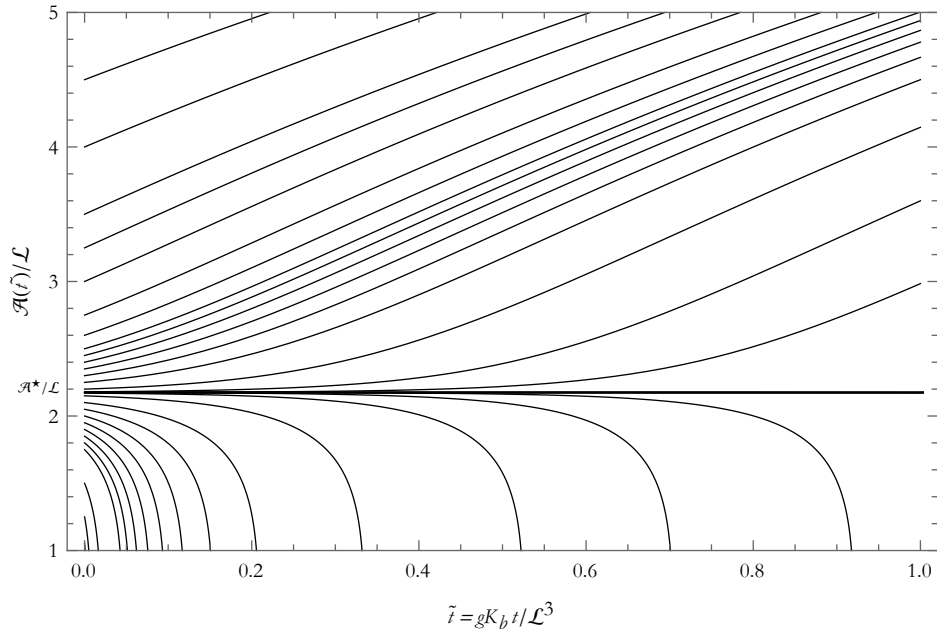


Figure 3.11: The time-dependent shape evolution $\mathcal{A}(\tilde{t})/\mathcal{L}$ as a function of the reduced time \tilde{t} . The critical arc-length is indicated with $\mathcal{A}^*/\mathcal{L} \approx 2.17$, which corresponds to an unstable equilibrium in the energy landscape $\mathcal{E}(\mathcal{A})$. The lowest value $\mathcal{A} = 1$ shown in this graph corresponds to the completely relaxed state.

3.3.2 Dynamics Due to a Potential Landscape, Including a Growth Term

The dynamics presented in figure 3.11 tell us that there is a *critical size* required for growth. One might ask: “How does it obtain the critical size in the first place?”. One effect that might contribute is *exocytosis*, which is a fascinating biological process by which a cell directs the contents of secretory vesicles out of the cell membrane and into the extracellular space. The vesicles *fuse* with the membrane (the ‘one-dimensional spine’ in this case), and thereby increase the size of the structure. It is now well understood that exocytosis of vesicles containing receptors plays a role in spine morphology, plasticity and enlargement [17; 13; 10; 9]. A cartoon of endocytosis (which is the converse of exocytosis) is shown in figure 3.12.

We will study the effect of exocytosis on shapes by means of the following differential equation:

$$\begin{aligned}\frac{d\mathcal{A}}{dt} &= k\mathcal{A} - g\frac{d\mathcal{E}}{d\mathcal{A}}, \\ \mathcal{A}(0) &= \mathcal{A}_0,\end{aligned}\tag{3.1}$$

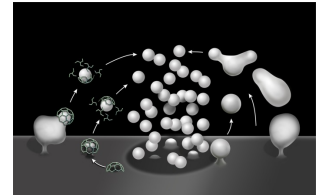


Figure 3.12: Cartoon illustrating clathrin-mediated (left) and clathrin-independent endocytosis (right) of synaptic vesicle membranes. Reproduced from Wu et al. [23].

where k is a *rate constant* with dimensions 1/time. In section 3.3.1 we required *one* parameter (*viz.* $\mathcal{A}(0)$), but we now have *two* independent parameters (*viz.* $\mathcal{A}(0)$ and a combination of k, g).

The reduced form of equation (3.1) is

$$\begin{aligned}\frac{d\tilde{\mathcal{A}}}{d\tilde{\tau}} &= \frac{1}{\tilde{\tau}}\tilde{\mathcal{A}} - \frac{d\tilde{\mathcal{E}}}{d\tilde{\mathcal{A}}}, \\ \tilde{\mathcal{A}}(0) &= \tilde{\mathcal{A}}_0,\end{aligned}\quad (3.2)$$

where $\tilde{\tau} = gK_b/k\mathcal{L}^3$ is a dimensionless time constant that tells us how fast vesicles fuse with the shape. For very long exocytosis times $\tilde{\tau} \gg 1$, exocytosis is a negligible process, but for $\tilde{\tau} \ll 1$, exocytosis dominates the shape dynamics (exponential growth). We have numerically solved equation (3.2) for various values of $\tilde{\tau}$ and $\tilde{\mathcal{A}}_0$, and recorded the evolution $\tilde{\mathcal{A}}(\tilde{\tau})$. We observe that there are two states the shape can be in: A *relaxed* state and a *grow* state. The *relaxed* state has $\tilde{\mathcal{A}}_\infty = 1$, a totally flat shape. The *grow* state grows *ad infinitum*. We have shown a phase portrait of these two states in figure 3.13. I think the “take home message” from this phase portrait is that the totally relaxed state $\tilde{\mathcal{A}}_0 = 1$ is able to get in the *grow* state as long as $\tilde{\tau} \lesssim e^{-4.3} \approx 0.0136$. Notice how this is markedly different from the shape dynamics shown in figure 3.11, in which we had to start with $\mathcal{A}_0 > \mathcal{A}^*$ to get in the *grow* state.

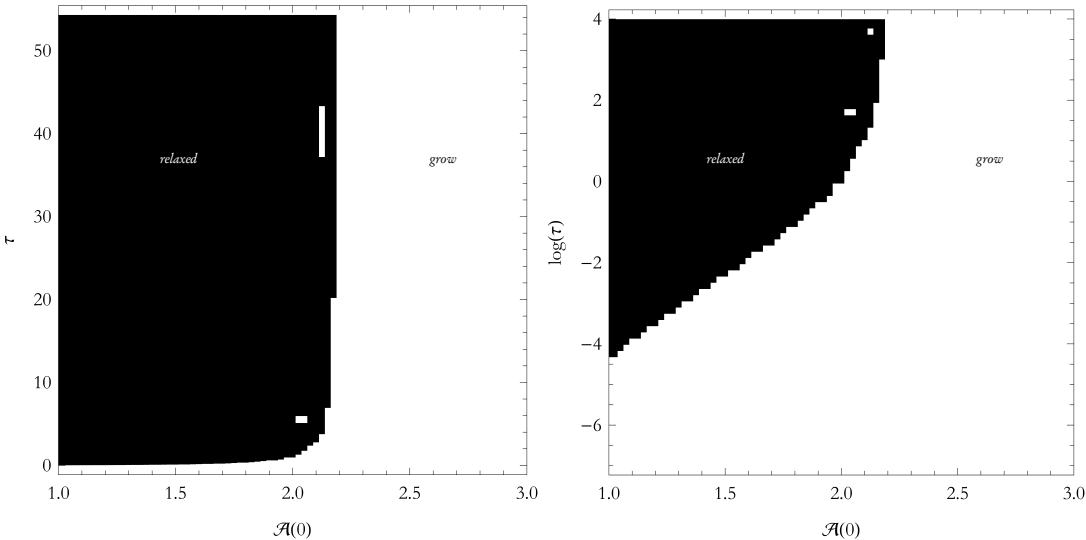


Figure 3.13: Phase portrait of the *grow* (white) and *relaxed* (black) states. The phase portrait depends on a combination of the arc-length at $t = 0, \mathcal{A}(0)$, and of the typical time τ of the exocytosis processes. The time τ and initial condition $\mathcal{A}(0)$ are numerically equivalent to their reduced counterparts, $\tilde{\tau}$ and $\tilde{\mathcal{A}}(0)$. N.B.: The log refers to the logarithm with base e .

3.3.3 Dynamics Due to a Potential Landscape, Including a Growth Term and a Growth Inhibition Term

As described in section 3.3.2, exocytosis is mediated by synaptic vesicles. Transportation of synaptic vesicles depends crucially, however, on the thickness of the neck. We propose a model in which transportation is inversely proportional to d_{neck} .⁷ The model that we propose is a competition between the

⁷In this model, transportation through a neck of thickness zero is impossible. In practice, the situation will be much more complicated, since the shape can deform in response to a force that the vesicles exert on the neck. We tacitly ignore such complications.

growth term which has $d_t \mathcal{A} \sim \mathcal{A}$ and a *growth inhibition term* which has $d_t \mathcal{A} \sim 1/d_{\text{neck}}$.⁸ The reduced form of the differential equation that we propose is:

$$\frac{d\tilde{\mathcal{A}}}{d\tilde{t}} = \frac{1}{\tilde{\tau}_{\text{ves.}}} \tilde{\mathcal{A}} - \frac{\tilde{\tau}_{\text{neck}}}{\tilde{\tau}_{\text{ves.}}} \frac{\mathcal{A}}{d_{\text{neck}}} - \frac{d\tilde{\mathcal{E}}}{d\tilde{\mathcal{A}}}, \quad (3.3)$$

where $\tilde{\tau}_{\text{neck}}$ is a measure for the time delay due to the neck constriction.⁹ Due to the divergence of the $1/d_{\text{neck}}$ term at $d_{\text{neck}} \rightarrow 0$, the shape will never be bigger than the point of self-crossing $\mathcal{A}_{\text{cross}} \approx 6.50$ (also discussed in section 3.2.3 on page 19). Depending on the steady state shape, \mathcal{A}_{∞} , we distinguish between three states:

complete growth The shape grows up to the point $d_{\text{neck}} \rightarrow 0$, so $\mathcal{A}_{\infty} \approx \mathcal{A}_{\text{cross}}$.

partial growth The shape grows, but $\mathcal{A}_{\infty} < \mathcal{A}_{\text{cross}}$.

relaxed The shape relaxes towards $\mathcal{A}_{\infty} = \mathcal{L}$ (i.e. $\tilde{\mathcal{A}}_{\infty} = 1$).

Differential equation (3.3) has been solved from the relaxed state $\tilde{\mathcal{A}}_0 = 1$ for various values of the time constants $\tilde{\tau}_{\text{ves.}}, \tilde{\tau}_{\text{neck}}$. The results of these computations have been shown in the phase portrait in figure 3.14.

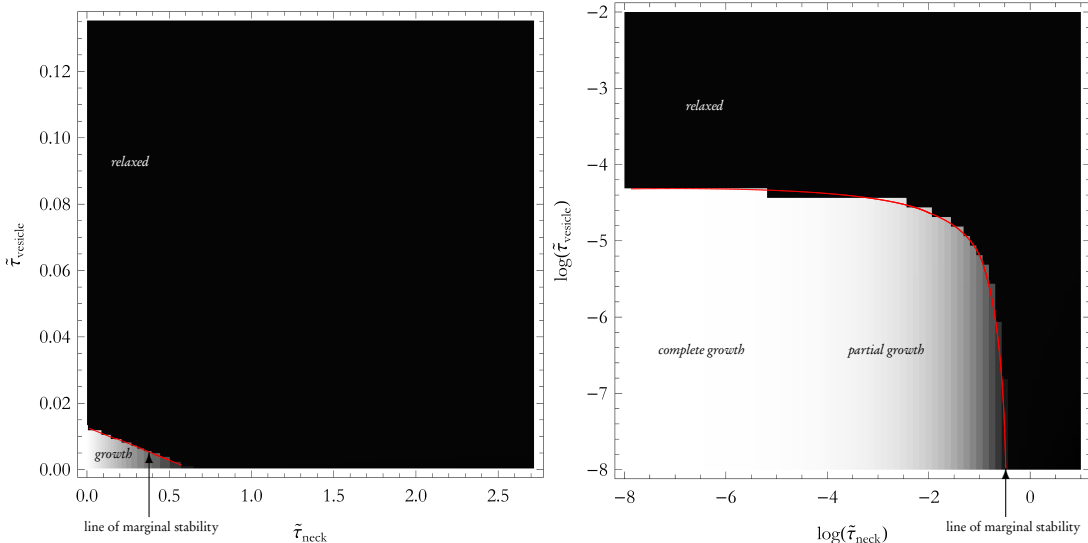


Figure 3.14: Color-coded phase diagrams for the various dynamical states that we encountered. Black corresponds to $\mathcal{A}_{\infty} = \mathcal{L}$, white corresponds to $\mathcal{A}_{\infty} = \mathcal{A}_{\text{cross}} \approx 6.50$. We have the states *relaxed* $\mathcal{A}_{\infty} = \mathcal{L}$, *partial growth* $\mathcal{L} < \mathcal{A}_{\infty} < \mathcal{A}_{\text{cross}}$ and *complete growth* ($\mathcal{A}_{\infty} = \mathcal{A}_{\text{cross}}$) for a range of time scales $\tilde{\tau}_{\text{vesicle}}$ due to exocytosis and $\tilde{\tau}_{\text{neck}}$ due to the neck obstruction on linear scales (left) and logarithmic scales (right). The lines of marginal stability (as defined in the text) are indicated in red. We used $\mathcal{A}(0) = \mathcal{L}$ for these phase portraits.

⁸The neck diameter has been presented in section 3.2.3 on page 19. As it turns out, there is, to an excellent degree of approximation, a linear relation between d_{neck} and \mathcal{A} . This relation (up to two decimals) is $d_{\text{neck}} \approx 0.78 - 0.12 \cdot \mathcal{A}$ with a coefficient of determination $R^2 = 0.997387$.

⁹The entire time delay is, of course, also dependent on d_{neck} , but $\tilde{\tau}_{\text{neck}}$ tells us the *weight* of this term. Depending on how much friction with the neck the synaptic vesicles experience, or on the strength of hydrodynamic forces, this time constant will be smaller or larger.

The phase portraits in figure 3.14—in particular the one with logarithmic scales—show beautifully that there is a region in the phase space $\{\tilde{\tau}_{\text{neck}}, \tilde{\tau}_{\text{ves.}}\}$ in which *growth* is possible from the relaxed state. In between the region of growth and the region of relaxation there is a *line of marginal stability*. The line of marginal stability has $\mathcal{A}(t) = \mathcal{A}(0)$. For time constants $\{\tilde{\tau}_{\text{neck}}, \tilde{\tau}_{\text{ves.}}\}$ smaller than those on the line of marginal stability, growth is possible, whereas for time constants larger than this, only relaxation is possible. For example, it is quite clear that $\log(\tilde{\tau}_{\text{neck}}) \gtrsim -0.30$ results in the *relaxed state*. On the line of marginal stability, and from the relaxed state, our dynamical equation reads

$$0 = \frac{1}{\tilde{\tau}_{\text{ves.}}} - \frac{\tilde{\tau}_{\text{neck}}}{\tilde{\tau}_{\text{ves.}}} \frac{1}{d_{\text{neck}}} - \frac{d\tilde{\mathcal{E}}}{d\mathcal{A}}.$$

In the above equation, we have $d_{\text{neck}}(\mathcal{A} = \mathcal{L}) \approx 2/3$ and $\tilde{\mathcal{E}}'(\mathcal{A} = \mathcal{L}) \approx 78$. We have, then, a linear relation between the *maximal* values of the time constants that still allow for growth:

$$0 = 1 - \frac{3}{2} \tilde{\tau}_{\text{neck}} - \tilde{\tau}_{\text{ves.}} \tilde{\mathcal{E}}'(\mathcal{L}). \quad (\text{marginal stability})$$

Numerically we find that the highest values of the time constants that allow for growth are: $\tilde{\tau}_{\text{neck}} = 2/3 \approx 0.67$, $\tilde{\tau}_{\text{ves.}} \approx 0.0128$. These two values are quite close to the values $\tilde{\tau}_{\text{neck}} \approx e^{-0.30} \approx 0.74$, $\tilde{\tau}_{\text{ves.}} \approx e^{-4.3} \approx 0.0136$ that we read off of figure 3.14.

3.4 Validity of Results

We have used a Fourier method to investigate the properties of a non-linear minimization problem. Because the analytical solution to this problem isn't known (to us), we have to use numerical methods to investigate the validity of the results. This section is a *triptych*: We will investigate the stability of our method in subsection 3.4.1, the convergence in subsection 3.4.2, and we will compare it with a finite difference method developed by Remy Kusters in subsection 3.4.3.¹⁰ We shall see that these three ways of investigating the validity of our results all lead to the same conclusion: The Fourier method that we have used is valid for analyzing curves that are subject to a bending energy.

3.4.1 Stability

All the data that has been presented thus far is obtained by built-in numerical Mathematica routines. It is therefore a good idea to *check* whether the solutions that Mathematica outputs are, indeed minimal solutions. In particular, other critical points—such as maxima or saddle-points—are possibilities that we will have to rule out. In order to proceed with this manner, we will introduce *perturbations* $\{\delta x, \delta y\}$ to our solution. If any perturbation increases the energy, we have indeed located a minimum, if not, then we haven't located a minimum.

The perturbations that we will use for the stability analysis are

$$\begin{aligned} \delta x_k &= \delta r_0 \sin q_k s, \\ \delta y_k &= \delta r_0 \cos q_k s, \end{aligned}$$

where $q_k = 2\pi k/\mathcal{A}$,¹¹ and $\delta r_0 : \delta r_0^2 = \delta x_k^2 + \delta y_k^2$ is a generalized amplitude of the perturbation. The normalization criterion $T(s)^2 = 1$ is now

$$0 = \cos q_k s \cdot x'(s) - \sin q_k s \cdot y'(s) + \frac{1}{2} q_k \delta r_0. \quad (3.4)$$

¹⁰The finite difference method intrinsically satisfies the boundary conditions, which is a major benefit to boundary value problems. For more information on the finite difference method, see the introductory survey on numerical methods by Heath [6].

¹¹These are the only allowed values of the wavenumber consistent with the boundary conditions on this interval of length \mathcal{A} , as we already found in section 2.5.

This expression tells us which perturbations $\{\delta x_k, \delta y_k\}$ are consistent with the normalization criterion; notice that which values δr_0 are allowed depends on the coordinate functions $x(s), y(s)$ as well as q_k . Now, integration over the interval $[-\mathcal{A}/2, +\mathcal{A}/2]$ gives

$$0 = \langle \cos q_k s | x'(s) \rangle - \langle \sin q_k s | y'(s) \rangle + \frac{1}{2} q_k \delta r_0,$$

where $\langle \Upsilon | \Pi \rangle \equiv \int_{-\mathcal{A}/2}^{+\mathcal{A}/2} \Upsilon(s) \Pi(s) ds$. The two inner products follow from the identities:

$$\begin{aligned} \left\langle \sin\left(\frac{2\pi ks}{\mathcal{A}}\right) \middle| \sin\left(\frac{2\pi ls}{\mathcal{A}}\right) \right\rangle &= \delta_{kl} \frac{1}{2} \mathcal{A}, \\ \left\langle \cos\left(\frac{2\pi ks}{\mathcal{A}}\right) \middle| \cos\left(\frac{2\pi ls}{\mathcal{A}}\right) \right\rangle &= \delta_{kl} \frac{1}{2} \mathcal{A}, \\ \left\langle \cos\left(\frac{2\pi ks}{\mathcal{A}}\right) \middle| \frac{\mathcal{L}}{\mathcal{A}} \right\rangle &= \mathcal{L} \text{sinc}\pi k, \end{aligned}$$

where δ_{ij} is the Kronecker delta and $\text{sinc}z \equiv \sin z/z$ is the sinc function. We have $\text{sinc}\pi k = 0$ since k is an integer. We find for the normalization criterion, equation (3.4), thus:

$$\begin{aligned} 0 &= \sum_l \alpha_l \frac{2\pi l}{\mathcal{A}} \left\langle \cos\left(\frac{2\pi ks}{\mathcal{A}}\right) \middle| \cos\left(\frac{2\pi ls}{\mathcal{A}}\right) \right\rangle + \sum_l \beta_l \frac{2\pi l}{\mathcal{A}} \left\langle \sin\left(\frac{2\pi ks}{\mathcal{A}}\right) \middle| \sin\left(\frac{2\pi ls}{\mathcal{A}}\right) \right\rangle + \frac{1}{2} \frac{2\pi k}{\mathcal{A}} \mathcal{A} \delta r_0 \\ &= \alpha_k \pi k + \beta_k \pi k + \delta r_0 \pi k. \end{aligned}$$

We find that the allowed perturbations are:

$$\delta r_0(k) = -(\alpha_k + \beta_k).$$

The energy variation due to a perturbation that constitutes two ‘sizes’ $\delta r_0(k), \delta \rho_0(\kappa)$ is:

$$\begin{aligned} \delta \mathcal{E}/K_b &= \int_{-\mathcal{A}/2}^{+\mathcal{A}/2} ds [2\delta x''(s) \cdot x''(s) + 2\delta y''(s) \cdot y''(s) + \delta x''(s)^2 + \delta y''(s)^2] \\ &= \int_{-\mathcal{A}/2}^{+\mathcal{A}/2} ds [-2(q_k^2 \delta r_0 \sin q_k s + q_\kappa^2 \delta \rho_0 \sin q_\kappa s) \cdot x''(s) - 2(q_k^2 \delta r_0 \cos q_k s + q_\kappa^2 \delta \rho_0 \cos q_\kappa s) \cdot y''(s) \\ &\quad + \delta r_0^2 q_k^4 + \delta \rho_0^2 q_\kappa^4 + 2\delta r_0 q_k^2 \delta \rho_0 q_\kappa^2] \\ &= (q_k^4 \delta r_0 \alpha_k + q_\kappa^4 \delta \rho_0 \alpha_\kappa) \cdot \mathcal{A} + (q_k^4 \delta r_0 \beta_k + q_\kappa^4 \delta \rho_0 \beta_\kappa) \cdot \mathcal{A} + (q_k^2 \delta r_0 + q_\kappa^2 \delta \rho_0)^2 \cdot \mathcal{A} \\ &= 2q_k^2 \delta r_0 q_\kappa^2 \delta \rho_0 \mathcal{A}, \end{aligned}$$

where in the last equality we used $\delta r_0 = -(\alpha_k + \beta_k)$. Again, this quantity should be positive for all k, κ .¹² We can plot this energy variation $\delta \mathcal{E}$ for $k = 1, \dots, 10$ and $\kappa = 1, \dots, 10$, which has been done in figure 3.15 for various values of \mathcal{A} .

For some of the higher modes, there are $\delta \mathcal{E}$ that are slightly negative, but we suspect that this is due to the tolerance in the normalization criterion $T(s)^2 = 1$.¹³ These negative energy variations have only been observed for $\mathcal{A} \leq 1.70$ and were < 1% of the total energy.

¹²Note that the energy variation $\delta \mathcal{E}$ is a *product* of the two ‘sizes’ $\delta r_0, \delta \rho_0$. Therefore a perturbation that constitutes of only one wavenumber will have no effect whatsoever on the energy.

¹³We allowed for a small variation δT in the normalization criterion, but here we assume that the normalization criterion is *exactly* satisfied. Also, we only enforced this normalization criterion on a finite set of points in the Mathematica programs. We suspect that two discrepancies between the Mathematica algorithm and this section allow for a small decrease in the energy.

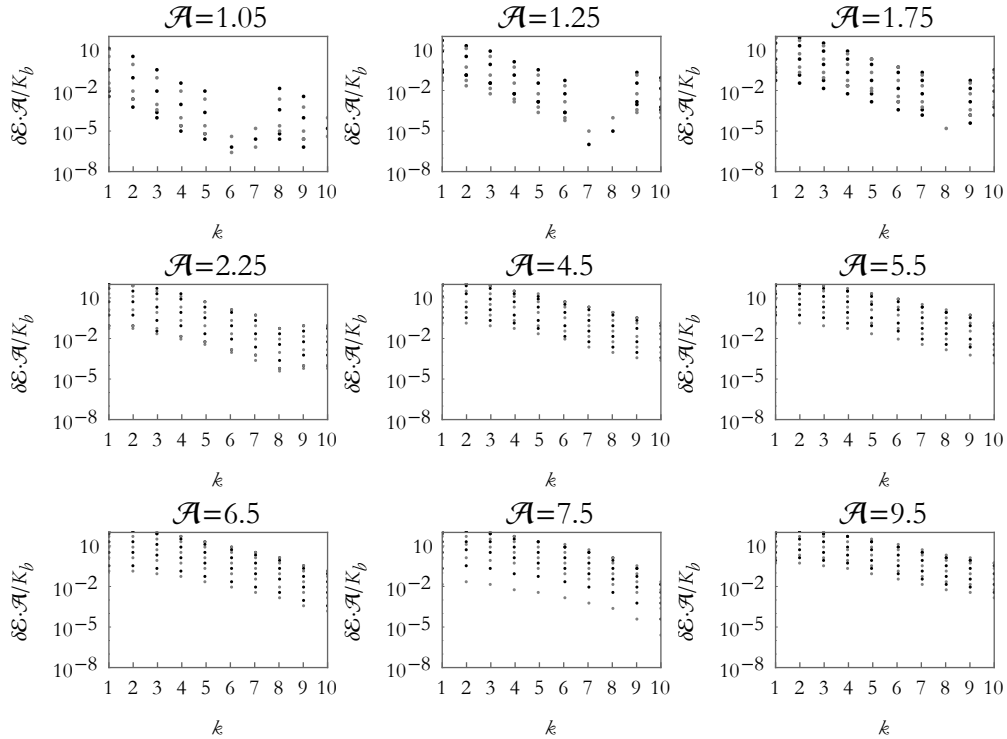


Figure 3.15: The dimensionless energy variations $\delta\mathcal{E} \cdot \mathcal{M}/K_b$ as a consequence of a perturbation $\{\delta x(s), \delta y(s)\}$ for various arc-lengths \mathcal{M} . This data has been generated from the same dataset as described in the rest of this chapter. The energy variations for $\mathcal{M} = 1.05, 1.25$ showed possible decreases in energy, which we discuss in footnote 13 and on page 28.

Because of the following facts combined, we suspect that the negative energy variations are a numerical anomaly:

1. The negative energy variations only affect < 1% of the total energy.
2. The negative energy variations have only been observed for small arc-lengths $\mathcal{M} \leq 1.70$.
3. The spectrum of energy variations $\delta\mathcal{E}(k)$ shows a pattern very similar to the energy spectrum of the shapes \mathcal{E}_k , namely exponential decay. The negative energy variations constitute an exception to this pattern.
4. There is a tolerance δT in the normalization criterion $T(s)^2 = 1$ used in the Mathematica scripts. Also, this normalization criterion is only enforced on a few coordinates in the interval. In this analysis, we ignore this tolerance and assume that the curve has been exactly normalized on every coordinate point.

To summarize: We regard the negative energy variations as a numerical anomaly, and conclude from this assumption that the solutions found in this chapter are indeed minimal solutions.

3.4.2 Convergence

Once we have a numerical approximation $r_n(s)$ to our problem—using a Fourier series with n modes, it is of interest to know how *close* this approximation is to ‘the solution’ $r_\infty(s)$.¹⁴

In order to analyze the convergence, we define the following *error measure*:

$$\Delta(n) \equiv \langle (|x_n| - |x_{n-1}|)^2 + (|y_n| - |y_{n-1}|)^2 \rangle,$$

where $\langle (\cdot) \rangle \equiv \mathcal{A}^{-1} \int ds (\cdot)$. The error measure tells us how much deviation there is between two successive approximations (with different numbers of modes). This function is plotted for various values of n and \mathcal{A} in figure 3.16. It is quite clear from this figure that the error measure is quickly decreasing—exponentially even—for $\mathcal{A} \geq 4.50$. For these values of \mathcal{A} , therefore, we can easily conclude that the series converges.

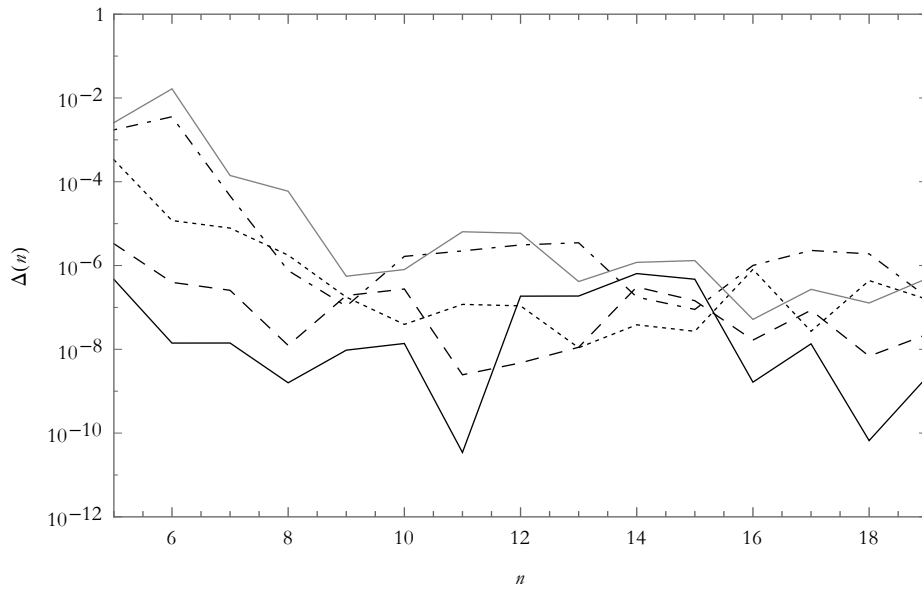


Figure 3.16: The error function $\Delta(n)$ for versus the number of modes n in a Fourier series on logarithmic scales. The various graphs correspond to: $\mathcal{A} = 1.02$ (—), $\mathcal{A} = 1.25$ (---), $\mathcal{A} = 2.25$ (···), $\mathcal{A} = 4.50$ (—·—), $\mathcal{A} = 6.50$ (—). This data has been generated by an average over 10 identical runs of the program, with the tolerance in the arc-length $\delta\mathcal{A} = 0.5\%$ and a normalization tolerance $\delta T = 0.1\%$.

For $\mathcal{A} < 4.50$ it is not immediately clear that the Fourier series converges: The error measure is small, but more or less constant. Someone might say:

If the error measure stabilizes to a certain value to, say, D , then we have introduced a systematic error D in our Fourier series!

In order to test this claim, we *decrease* the tolerance δT in the normalization criterion, to see whether this has any effect.¹⁵ Indeed, if we compare the plots corresponding to $\delta T = \{10^{-4}, 10^{-5}, 10^{-6}\}$, we

¹⁴Which functions can be approximated by a Fourier series (in a point-wise manner) is dictated by the *Dirichlet conditions* [19], which are fulfilled in our case. We can then safely say that the function we are trying to approximate is *equal* to its Fourier series (if we take into account all terms, that is).

¹⁵Just to clarify: *Decreasing* the tolerance in the normalization criterion makes the normalization criterion *more accurately* satisfied. It is also much more computationally expensive, and the value $\delta T = 10^{-4}$ is a compromise between speed and accuracy.

find that the $\delta T = \{10^{-5}, 10^{-6}\}$ also show exponential decay. This leads us to conclude that there is indeed convergence if for these values of δT . Also, we found that the solutions corresponding to $\delta T = \{10^{-5}, 10^{-6}\}$ are equivalent to the solution using $\delta T = 10^{-4}$ (apart from some numerical errors, which are in the order of 10^{-8} for $\delta T = 10^{-4}$). This, then, leads us to conclude that the solution found with $\delta T = 10^{-4}$ is also a solution that converges to the correct result.

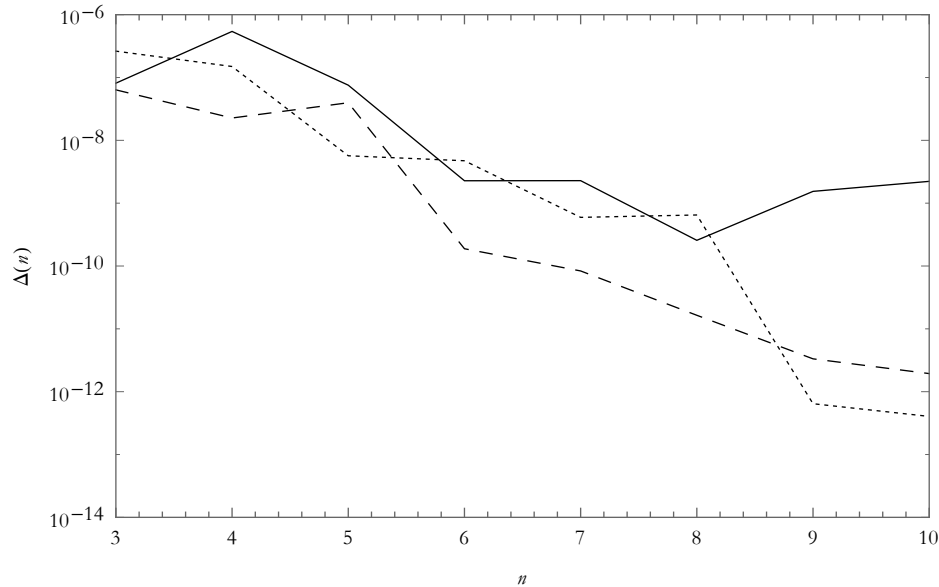


Figure 3.17: The error measure $\Delta(n)$ versus n for $\mathcal{A} = 1.05$ on logarithmic scales. The different graphs correspond to different values of δT : $\delta T = 10^{-4}$ (—), 10^{-5} (---), 10^{-6} (···). The tolerance in the arc-length $\delta \mathcal{A} = 0.5\%$.

3.4.3 Comparison with Finite Difference Method

In order to compare the results found by a finite difference method [6] developed by Remy Kusters with those examined in this written work, we will superimpose the shapes of the two methods.¹⁶ We will superimpose the shapes of the two methods for values of the arc-length \mathcal{A} that correspond to different types of the morphology. The values we have chosen are: $\mathcal{A} = 1.05, 1.75, 2.25, 3.25, 3.75, 4.50, 6.50, 7.50$. The superimposed shapes have been shown in figure 3.18. It is clear from this figure that the shape morphologies are the same, although the method in the finite difference scheme produces a slightly lower energy.¹⁷

¹⁶Henceforth we shall simply speak of “the finite difference method” and “the Fourier method” if we are referring to respectively “the finite difference method developed by Remy Kusters” and “the Fourier method examined in this written work”.

¹⁷Which is to be expected, since the finite difference scheme (as used here) minimizes w.r.t. 1000 coordinates, whereas the Fourier method minimizes w.r.t. 10 coefficients.

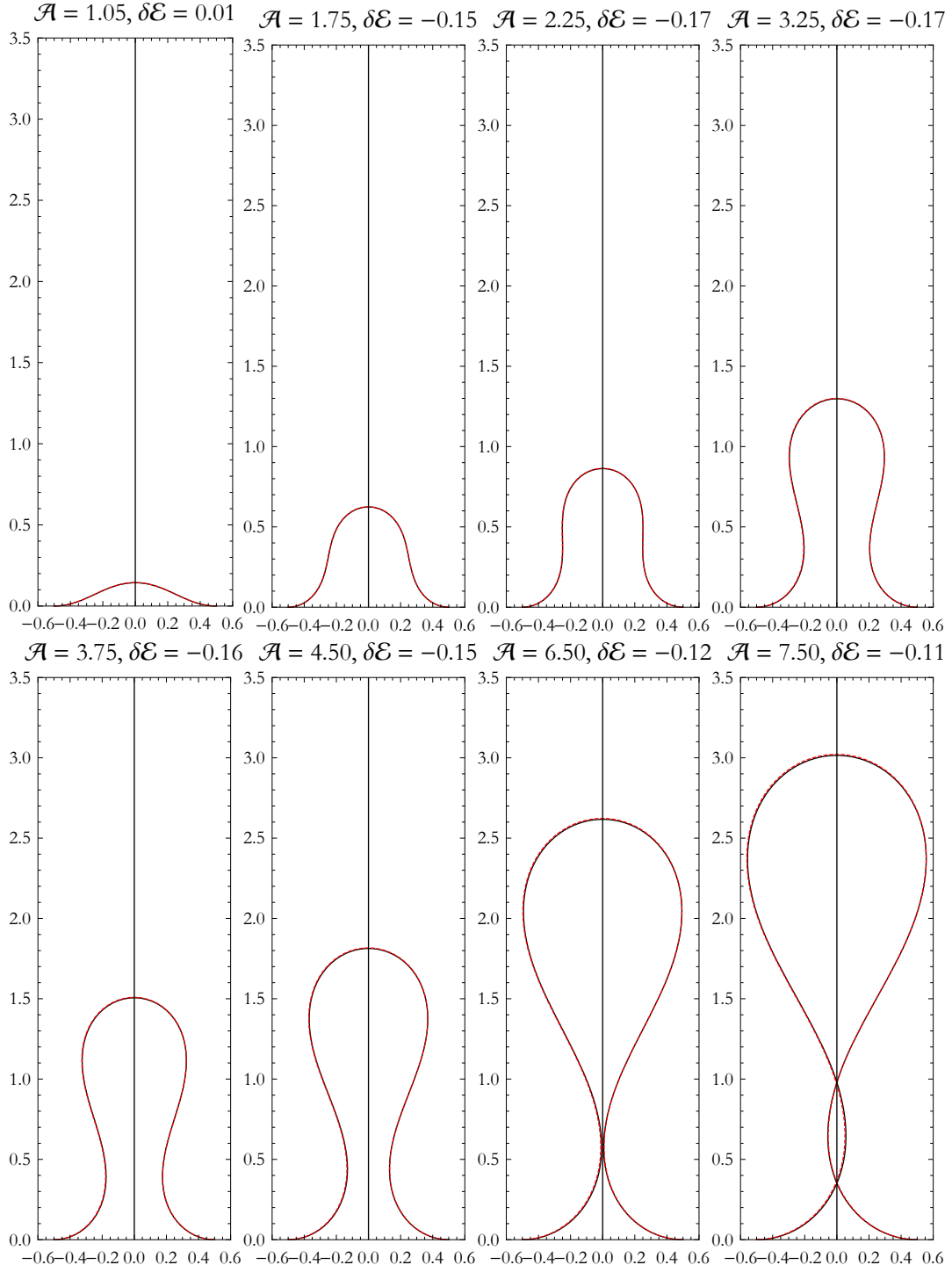


Figure 3.18: Superimposed shapes of those using the Fourier method (—) and those using the finite difference method (—). Also shown is the energy difference $\delta\mathcal{E} \equiv \mathcal{E}_{\text{finite difference}} - \mathcal{E}_{\text{Fourier}}$. The shapes corresponding to the Fourier method are the same as those shown in figures 3.2, 3.3. The shapes corresponding to the finite difference calculations have been generated with 1000 points in the interval and 5000 iteration steps.

Chapter 4

Conclusion and Outlook

In section 1.1 we formulated several research questions. To my great joy, we have been able to answer all of these research questions. In the section 4.1 below, we summarize the answers to these research questions. Then, in section 4.2 we mention some of the aspects that we have overlooked or omitted.

4.1 Summary of Findings

In this written work, we discuss curves that are subject to a *bending energy*. We implement this energy using a *Canham-Helfrich* energy functional. We have proposed a method, based on a Fourier series, to analyze various properties of such bending beams subject to a specific set of boundary conditions. These boundary conditions are inspired by the geometry of dendritic spines.

We found that built-in solvers of Mathematica are suitable for handling this variational problem, which we established by investigating the effect of a perturbation on the solution. Alongside the stability and convergence, we have also shown that a finite difference method produces the same results.

Using this method, we were able to generate a sequence of beautiful *growth shapes* by increasing the arc-length $\tilde{\mathcal{A}}$. These shapes showed a distinct neck and head from arc-lengths $\tilde{\mathcal{A}}_{\text{neck}} \gtrsim 2.25$, and was self-crossing at the location of the neck from $\tilde{\mathcal{A}}_{\text{cross}} \approx 6.50$. We proposed a toy-model to describe the head width d_{head} , neck width d_{neck} , and the ratio $d_{\text{head}}/d_{\text{neck}}$ as a function of the arc-length of the curve. The linear models for $d_{\text{head}}, d_{\text{neck}}$ described the data to an excellent degree. The ratio $d_{\text{head}}/d_{\text{neck}}$ diverges at $\tilde{\mathcal{A}}_{\text{cross}}$ and scales as $1/(\tilde{\mathcal{A}}_{\text{cross}} - \tilde{\mathcal{A}})$. Alongside the head and neck width, we also computed the shape height and shape two-dimensional volume $\int |dy| x|$. For both the shape height and the volume we were able to present toy-models that describe the scaling behavior of these quantities.

Due to the linear nature of the energy functional that we are describing, it is possible to write the energy \mathcal{E}_k of a *single mode* k . It so appears that this energy spectrum showed *exponential decay* as a function of k -or, in other words—there is a *typical length-scale* associated with the shapes. This typical length-scale is an increasing function of $\tilde{\mathcal{A}}$. For large values of $\tilde{\mathcal{A}}$ the typical length-scale is $\approx \frac{1}{2}\tilde{\mathcal{A}}$.

Using heuristics, we presented several simple models for *shape dynamics* based on a first-order differential equation. As anticipated, we found that there is a *critical arc-length* $\tilde{\mathcal{A}}^* \approx 2.17$ associated with the energy landscape. If we only take into account these energetic effects, then a shape with arc-length smaller than the critical arc-length *relaxes* to its ground-state $\tilde{\mathcal{A}} = 1$. *Au contraire*, for arc-lengths larger than the critical arc-length the shape *spontaneously grows*. The critical arc-length $\tilde{\mathcal{A}}^*$ is an *unstable equilibrium* of the energy landscape.

We also presented two additional—more interesting—models for shape dynamics. These two models were inspired by exocytosis, a biological phenomenon, and constriction of vesicles that perform this exocytosis in the neck. These two competing effects resulted in different *states* the shape could be in.

We found that the shape is able to grow to a stable structure from the relaxed state—as long as the time constants associated with these processes are sufficiently small. We also found numerical values for these time constants.

4.2 Outlook

There are several aspects of curves that resist bending that we have purposefully or accidentally omitted.

One aspect that is interesting to investigate is at the core of the method we used: The tolerance in the normalization criterion.¹ This is a rather artificial method of enforcing the normalization criterion. Much more at the heart of the physis involved would be to introduce a *line tension*. This is something we will try to use when modelling membranes, actually.

It would be of some use to expand the work on shape dynamics. For example: I can imagine that it is useful to include some simple hydrodynamics (since most biological systems live in an aqueous environment) or inertia. This type of model is interesting when we think of microtubuli, for example, that live near a hole.

We have examined curves that have a certain, definite arc-length, *no matter* what the required forces are. No system “Under the Heavens” is able to do this, of course. Often the forces are delivered through a pressure. It is of great interest to analyze the effect of such a pressure. This type of problem can be tackled using thermodynamics and statistical physics.

Also, we haven’t thoroughly examined the influence of thermal fluctuations. For instance, it might be interesting to look at the various shapes that arise if we allow these fluctuations.

More interestingly than all the above points is to make models of *two-dimensional structures*. This will be the main goal of the rest of my graduate work.

¹Enforcing the normalization criterion gave us a lot of headaches. I discussed some of the problems regarding this in sections 3.4.1 and 3.4.2.

Bibliography

- [1] H. Felgner, R. Frank, and M. Schliva. *Journal of Cell Science*, 109, 1996.
- [2] Maria Fischer, Stefanie Kaech, Darko Knutti, and Andrew Matus. Rapid actin-based plasticity in dendritic spines. *Neuron*, 20(5):847–854, 1998.
- [3] F. Gittes, B. Mickey and J. Nettleton, and J. Howard. *Journal of Cell Biology*, 120, 1993.
- [4] Zhou Haijun, Zhang Yang, and Ou-Yang Zhong-can. Bending and base-stacking interactions in double-stranded dna. *Physical Review Letters*, 82(22), 1998.
- [5] Kristen M. Harris and John K. Stevens. Dendritic spines of ca1 pyramidal cells in the rat hippocampus: Serial electron microscopy with reference to their biophysical characteristics. *The Journal of Neuroscience*, 9, 1989.
- [6] Michael T. Heath. *Scientific Computing: An Introductory Survey*. McGraw Hill, 2 edition, 2002.
- [7] Wolfgang Helfrich. Elastic properties of lipid bilayers: theory and possible experiments. *Zeitschrift für Naturforschung. Teil C: Biochemie, Biophysik, Biologie, Virologie*, 1973.
- [8] Pirta Hotulainen and Casper C. Hoogenraad. Actin in dendritic spines: Connecting dynamics to function. *Journal of Cell Biology*, 189(4):619–629, May 2010. ISSN 1540-8140. doi: 10.1083/jcb.201003008.
- [9] Matthew J. Kennedy, Ian G. Davison, Camenzind G. Robinson, and Michael D. Ehlers. Syntaxin-4 defines a domain for activity-dependent exocytosis in dendritic spines. *Cell*, 141(3):524 – 535, 2010. ISSN 0092-8674. doi: <http://dx.doi.org/10.1016/j.cell.2010.02.042>. URL <http://www.sciencedirect.com/science/article/pii/S0092867410001959>.
- [10] Charles D. Kopec, Bo Li, Wei Wei, Jannic Boehm, and Roberto Malinow. Glutamate receptor exocytosis and spine enlargement during chemically induced long-term potentiation. *The Journal of Neuroscience*, 26(7):2000–2009, 2006. doi: 10.1523/JNEUROSCI.3918-05.2006. URL <http://www.jneurosci.org/content/26/7/2000.abstract>.
- [11] M. Kurachi, M. Hoshi, and H. Tashiro. *Cell Motility and the Cytoskeleton*, 30, 1995.
- [12] Lev Landau. On the theory of phase transitions. *Ukr. J. Phys.*, 53, Special Issue, 2008. Translated and reprinted from Landau L.D. "Collected Papers".
- [13] Hiroshi Makino and Roberto Malinow. {AMPA} receptor incorporation into synapses during ltp: The role of lateral movement and exocytosis. *Neuron*, 64(3):381 – 390, 2009. ISSN 0896-6273. doi: <http://dx.doi.org/10.1016/j.neuron.2009.08.035>. URL <http://www.sciencedirect.com/science/article/pii/S0896627309006758>.

- [14] Andrew Matus. Actin-based plasticity in dendritic spines. *Science*, 290(5492):754–758, 2000.
- [15] Sylvester T. McKenna, Joseph G. Kunkel, Maurice Bosch, Caleb M. Rounds, Luis Vidali, Lawrence J. Winship, and Peter K. Hepler. Exocytosis precedes and predicts the increase in growth in oscillating pollen tubes. *The Plant Cell Online*, 21(10):3026–3040, 2009. doi: 10.1105/tpc.109.069260.
- [16] B. Mickey and J. Howard. *Journal of Cell Biology*, 130, 1995.
- [17] Enrica Maria Petrini, Jiuyi Lu, Laurent Cognet, Brahim Lounis, Michael D. Ehlers, and Daniel Choquet. Endocytic trafficking and recycling maintain a pool of mobile surface {AMPA} receptors required for synaptic potentiation. *Neuron*, 63(1):92 – 105, 2009. ISSN 0896-6273. doi: <http://dx.doi.org/10.1016/j.neuron.2009.05.025>. URL <http://www.sciencedirect.com/science/article/pii/S0896627309004000>.
- [18] Rob Phillips, Jane Kondev, Julie Theriot, and Hernan G. Garcia. *Physical Biology of the Cell*. Garland Science, 2013.
- [19] K. F. Riley and M. P. Hobson. *Essential Mathematical Methods for the Physical Sciences*. Cambridge University Press, 2011.
- [20] Michael Stone and Paul Goldbart. *Mathematics for Physics*. Cambridge University Press, 2009.
- [21] Takuro Tojima, Hiroki Akiyama, Rurika Itofusa, Yan Li, Hiroyuki Katayama, Atsushi Miyawaki, and Hiroyuki Kamiguchi. Attractive axon guidance involves asymmetric membrane transport and exocytosis in the growth cone. *Nat Neurosci*, 10(1):58–66, January 2007. ISSN 1097-6256.
- [22] P. Venier, A. C. Maggs, M. F. Carlier, and D. Pantaloni. *Journal of Biological Chemistry*, 269, 1994.
- [23] Y. Wu, E. O’Toole, M. Girard, B. Ritter, M. Messa, X. Liuand, P. McPherson, S. Ferguson, and P. De Camilli. A dynamin 1-, dynamin 3- and clathrin-independent pathway of synaptic vesicle recycling mediated by bulk endocytosis. *eLife*, 2014. doi: 10.7554/eLife.01621.
- [24] Karen Zito, Graham Knott, Gordon MG Shepherd, Shirish Shenolikar, and Karel Svoboda. Induction of spine growth and synapse formation by regulation of the spine actin cytoskeleton. *Neuron*, 44(2):321–334, 2004.

Appendix A

Minimization Algorithm

We use built-in minimization algorithms in Mathematica in order to find the critical points of the energy functional. The minimization algorithm isn't all there is to it, however. For one thing, the Fourier series has been programmed into these scripts, alongside the constraints on the tangent vector and on the total arc-length.

The procedure consist of calling a hierarchy of scripts, which are initiated by “`LoopStructureOneValueForVector \mathfrak{A}` ” command. This `LoopStructureOneValueForVector \mathfrak{A}` script takes the input values described below.

Input

\mathfrak{A}	A list consisting of the values of the arc-length.
δT	A scalar that measures the ‘resistance’ to local stretch and contraction. This can be regarded as an effective elastic constant. Lower δT results in a higher elastic constant. This value of δT is only evaluated at a finite set of randomly selected coordinates.
$\delta \mathcal{A}$	A scalar that measures the ‘resistance’ to global stretch and contraction. The arc-length of the curve is constrained to deviate an amount $\delta \mathcal{A}$ from the inputted values \mathfrak{A} .
\mathcal{L}	The horizontal distance between the points where the boundary conditions are constrained. I used $\mathcal{L} = 1$ everywhere.
α	The symbol that is used for the Fourier coefficients α_k of the $x(s)$. Is completely arbitrary and up to personal preference, of course.
β	The symbol that is used for the Fourier coefficients β_k of the $y(s)$.
AO	The vector containing an initial guess for the α_k . The loop structure assumes a <i>growth-process</i> , such that each new iteration the AO is updated to the newest solution. I used very poor initial guesses, but that resolved itself after one iteration step. Notice that the number of orders is derived from the amount of elements of this vector!
BO	The vector containing an initial guess for the β_k . Notice that the number of orders is derived from the amount of elements of this vector!

- NRuns* The number of identical runs per value of \mathcal{A} . It is not necessary to make this very high, unless you want excellent statistics (the results for the Fourier coefficients don't differ a lot between runs). I used *NRuns*= 10, but I think 5 would already suffice.
- ParentFolder* The folder in which the scripts are located that are called, namely: “`makeFunctions-AndFunctionals.m`”, “`makeCoefficientsAndLists.m`” and “`makeLoopStructureForOneValueA.m`”.
- OutputFolder* The folder in which the data will be stored. Notice how I tried to circumvent overwriting of previous results by automatically creating a folder named “[year]-[month][day] [hour].[minute]”, where the metrics [...] are assumed to be self-evident. This same folder is used for every element of \mathfrak{A} , where the [hour] and [minute] are determined from the point of initiation of the loop structure. Hence, the user can simply leave *OutputFolder* as is, and the risk of overwriting results is negligible (they have to take place within the same minute).

Output

The output of the script falls in two categories: Information that is displayed in the notebook (but not stored or exported), and information that is saved to the folder specified by *OutputFolder*.

Information Displayed on the Notebook In the following order, several metrics are displayed on the notebook:

- T* The computational time for the *NRuns* number of runs, for one value of \mathcal{A} .
- OutputFolder/A=[A]* The specific folder in which the data is placed. I programmed the script such that $[\mathcal{A}]$ is a number with two decimals, so the folder will appear nicely ordered on a Windows system.
- $\mathcal{E}_{\text{last run}}$ The total energy of the last run.
- $\Delta_{\mathcal{A}}$ The relative error in the arc-length constraint, defined as follow: $\frac{1}{\mathcal{A}} \int ds |\mathbf{T}| - 1$.

Information that is Stored in *OutputFolder* In *OutputFolder*, there are subfolders placed for each value of \mathcal{A} . Each of these subfolders contains the following .dat files:

- Ak.dat* The Fourier coefficients α_k . Each column contains the coefficients to one run.
- Bk.dat* The Fourier coefficients β_k . Each column contains the coefficients to one run.
- Ek.dat* The energies per mode \mathcal{E}_k . Each column contains the coefficients to one run.
- Ekx.dat* The energies in the x -direction per mode \mathcal{E}_k^x . Each column contains the coefficients to one run.
- Eky.dat* The energies in the y -direction per mode \mathcal{E}_k^y . Each column contains the coefficients to one run.

Furthermore, there is information contained in the header to each of these .dat files. The following information is placed there:

- A* The total arc-length \mathcal{A} .

<i>deltaT</i>	The tolerance δT in the normalization criterion (as used in the program).
<i>deltaA</i>	The tolerance $\delta \mathcal{A}$ in the arc-length constraint (as used in the program).
<i>NRuns</i>	The number of identical runs. This is the number of columns in each .dat file.
<i>n</i>	The number of Fourier modes used in the computation.
<i>L</i>	The distance between the boundary points \mathcal{L} .
<i>Comp. time</i>	The computational time for the <i>NRuns</i> runs, for this particular value of \mathcal{A} .

Appendix B

Plateau Regime in Energy Spectrum

In section 3.2.2 on page 17 we analyzed the power spectral density, and observed that (for a large part of the spectrum) the energy per mode \mathcal{E}_k decayed exponentially with k . However, we also observed that there appeared to be a *plateau* in the energy per mode for high values of k . If this plateau is a numerical difficulty without physical meaning, or if the plateau disappears as soon as we perform more accurate computations, then we are in luck. If such a plateau *does* has physical meaning, then we are *not* allowed to cut-off the energy spectrum.¹ It is therefore important to convince ourselves which of these statements is true. In this appendix, therefore, we will study this plateau in some detail.

We have used computations with $\delta\mathcal{A} = 10^{-3}$, $\delta T = 10^{-4}$ and one run of the program (*NRUNS=1*) for number of modes $n = 4 \dots 19$.² We study the energy spectra corresponding to $\mathcal{A} = 1.05, 1.25, 2.25, 4.50, 6.50$. These arc-lengths correspond to shapes that all have more or less distinct morphologies—and we therefore expect that we can gain sufficient understanding through this limited set.

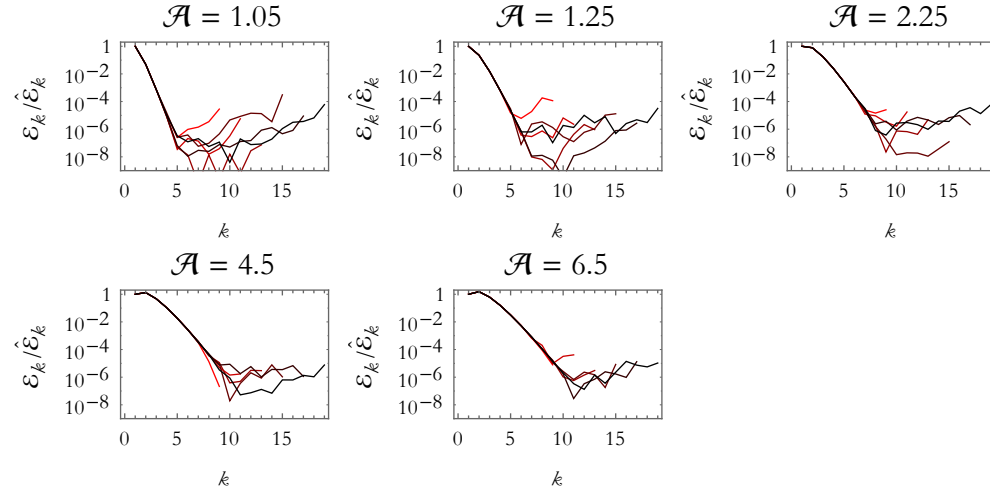


Figure B.1: The normalized energy spectrum for various values of \mathcal{A} and number of modes $n = 9, 11, 13, 15, 17, 19$ (red corresponds to $n = 9$, black to $n = 19$ and the other n to intermediate colors)

¹This is the case because—even though the energy per mode in that part may be very low—the total energy of an infinitely large plateau is itself infinite. In this chapter, we will make the case that the plateau is an unphysical result, and can be dismissed on the basis of this unphysicality.

²For the sake of clarity we only present the subset of the results corresponding to $n = 9, 11, \dots, 17, 19$. We found that the full set of computations gave rise to similar conclusions as can be found from the smaller dataset as presented in this chapter.

The normalized energy spectra for various values of n have been shown in figure B.1. The first observation that we can make is that the plateau is present for all values of n . That being said, the plateau shifts to higher values of k for higher values of n . Below, in table B.1, we have tabulated estimations of the start of the plateau regime for the various values of \mathcal{A} and n . Alongside this, we have also indicated the approximate height of the plateau.

Table B.1: The mode number k where the plateau starts and the energy of the plateau \mathcal{E} for various values of the total number of modes n and the arc-length \mathcal{A} .

\mathcal{A}	n																	
	k	$n = 9$	\mathcal{E}	k	$n = 11$	\mathcal{E}	k	$n = 13$	\mathcal{E}	k	$n = 15$	\mathcal{E}	k	$n = 17$	\mathcal{E}	k	$n = 19$	\mathcal{E}
1.05	5	10 ⁻⁵		5	10 ⁻⁶		5	10 ⁻⁵		5	10 ⁻⁸		5	10 ⁻⁷		5	10 ⁻⁷	
1.25	5	10 ⁻⁴		6	10 ⁻⁶		7	10 ⁻⁶		6	10 ⁻⁶		7	10 ⁻⁶		6	10 ⁻⁶	
2.25	6	5×10^{-5}		6	10 ⁻⁵		9	10 ⁻⁶		10	10 ⁻⁷		8	10 ⁻⁶		8	10 ⁻⁶	
4.50	—	—		10	10 ⁻⁶		10	10 ⁻⁶		10	10 ⁻⁶		9	10 ⁻⁶		11	10 ⁻⁷	
6.50	—	—		9	5×10^{-5}		9	10 ⁻⁶		11	10 ⁻⁶		11	10 ⁻⁶		12	10 ⁻⁶	

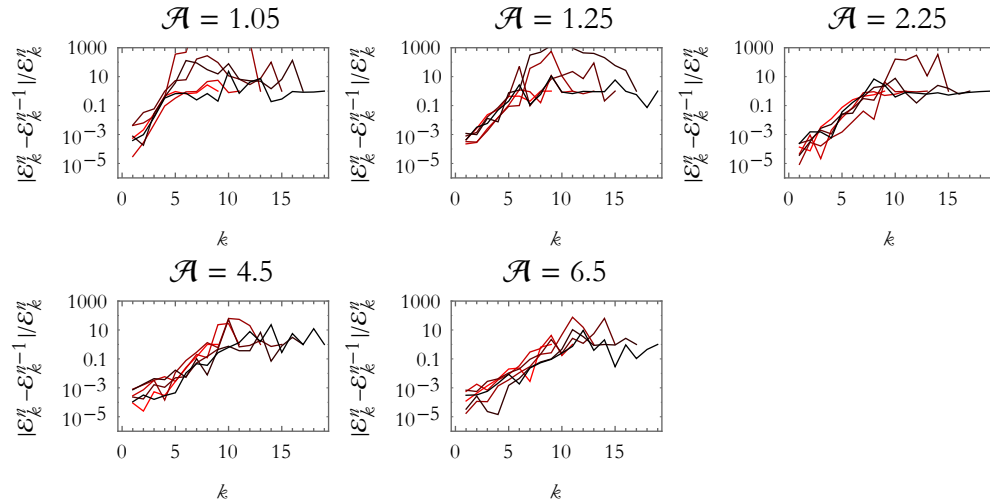


Figure B.2: The relative error in successive approximations $\varphi_n(k)$ as defined in the text. The relative error $\varphi_n(k)$ has been plotted for modes $n = 9, 11, 13, 15, 17, 19$ (red corresponds to $n = 9$, black to $n = 19$ and the other n to intermediate colors)

Another aspect of the plateau regime that is immediately evident is its *variability*. This can be seen in the energies in the plateau part of the spectrum (as found in table B.1),³ but it can most strikingly be shown by visualizing the relative error per successive approximation $\varphi_n(k)$, defined as follows: $\varphi_n(k) \equiv |\mathcal{E}_k^n - \mathcal{E}_k^{n-1}|/\mathcal{E}_k^n$ (here \mathcal{E}_k^n is the energy per mode with n modes in total). This function is plotted in figure B.2 for the same set of values for \mathcal{A} and n used in the rest of this chapter. Loosely speaking, this metric is small if the two approximations are ‘close’ to each other, and it will be large if the successive

³I am referring here to the fact that approximations with different values of n have plateau energies that differ by multiple orders of magnitude—that is a strong variability, if ever there was one.

approximations are not ‘close’ to each other. In particular, if this function (for some k) is larger than unity, even an optimist would say that the approximation is useless.

For values of k outside of the plateau regime, the relative error $\varphi_n(k)$ is satisfactory—in the order of $0.1\% - 1\%$. However, the relative error $\varphi_n(k)$ is a rapidly increasing function of k —particularly the plateau regime displays catastrophically large errors. *What does this tell us?* It basically tells us that we cannot trust a thing of the energy spectrum in the plateau regime. It would be foolish, therefore, to conclude that the plateau has physical relevance on the basis of these computations.⁴

In this appendix, we have made the case that the plateau regime in the energy spectrum can be dismissed as an unphysical result. We have made this plausible by showing that the results in that part of the spectrum do not converge. As such, the plateau is in itself not even numerically stable. In summary: We argue that the plateau regime in the energy spectrum can safely be ignored.

⁴There is another reason why we wouldn’t expect this. There are, namely, only two intrinsic length-scales in the system: The arc-length \mathcal{A} and the spacing \mathcal{L} of the boundaries. These two length-scales express themselves in the bump at $k \approx 1$ and in the slope of the energy spectrum. We wouldn’t expect, therefore, there to be other bumps or plateaus in the energy spectrum.